Intra- and intersegmental neural network architectures determining rhythmic motor activity in insect locomotion

Azamat Yeldesbay[a,b,*] and Silvia Daun[b,a,**]

[a] *University of Cologne, Institute of Zoology, Heisenberg Research Group of Computational Neuroscience - Modeling Neural Network Function*
Zülpicher Str. 47b, 50674 Cologne, Germany
[b] *Research Centre Jülich, Institute of Neuroscience and Medicine (INM-3)*
Cognitive Neuroscience, 52425 Jülich, Germany
[*] *Corresponding author: azamat.yeldesbay@uni-koeln.de (A. Yeldesbay)*
[**] *Principal corresponding author: s.daun@fz-juelich.de (S.Daun)*

Published in October 2019 in
Communications in Nonlinear Science and Numerical Simulation, Volume 82, 105078,
DOI: https://doi.org/10.1016/j.cnsns.2019.105078

Abstract

The coordinated movement of the extremities of an animal during locomotion is achieved by the interaction between groups of neurons called central pattern generators (CPGs). In the absence of any sensory input this network creates a stable rhythmic motor activity that is essential for a successful coordination between limbs. Studying the structure and the interaction between different parts of the CPG network is therefore of particular interest.

This work is motivated by recent experimental results reported by Mantziaris et al. (2017). By chemically activating both isolated and interconnected deafferented thoracic segments (ganglia) of the stick insect Mantziaris et al. (2017) analyzed the interactions between contralateral networks that drive the levator-depressor muscle pairs, which are responsible for the upward-downward movement of the legs. The results of the experimental analysis showed that intrasegmental phase relations differ between isolated segments. In particular, in isolated segments where the control networks of the middle and hind legs reside, i.e. in the meso- and metathoracic ganglia, the phase relations between activities of the contralateral depressor motoneurons were in-phase and anti-phase, respectively. Moreover, the phase relations switched to in-phase and stabilized when the ganglia were interconnected.

Using the phase reduction of an intersegmental network model of stick insect locomotion presented in our previous work (Yeldesbay et al. (2018)), we built a reduced model of the intra- and intersegmental network controlling levator-depressor activity in the meso- and metathoracic ganglia. By examining the intra- and intersegmental phase differences in the model we identified the properties of the network couplings that replicate the results observed in the experiments. We applied the theoretical analysis to escape type CPGs and revealed a set of possible contra- and ipsilateral synaptic connections. Finally, we defined general features of the couplings between CPGs of any type that maintain the phase relations observed in the experiments.

Keywords: Central pattern generators, Phase reduction, Coupled phase oscillators

1 Introduction

During locomotion the body parts of an animal move in a coordinated way [1]. The coordination of different legs of a walking insect is provided by a rhythmically coordinated activation of different groups of muscles [2, 3, 4]. The activity of these different muscle groups is controlled by neural networks called *central pattern generators* (CPG) [5, 6]. In combination with sensory and central descending inputs, a network of interconnected CPGs generates rhythmic motor output, thereby providing variable and adaptable locomotion [7, 8].

Previously, it was shown that a network of interconnected CPGs is able to generate rhythmic activity even without any sensory input [9, 10, 11]. This rhythmic activity is called *fictive locomotion* and takes place either spontaneously or when the network is chemically activated. The activity pattern generated by an isolated neural circuit during fictive locomotion does not necessarily resemble the one observed in real walking of the animal, and is modified by signals from other parts of the larger network that control the locomotion. Nevertheless, these underlying rhythmic activities are characterized by the couplings between the CPGs that build the core of the whole network. Therefore, fictive locomotion is considered to be the mechanism underling the generation of real locomotion and studying the structure of the CPG network is crucial for understanding locomotion in general. Despite of this fact, a systematic investigation of the structure of the neural circuit of the insect walking system that produces the fictive motion is still lacking.

Recent studies addressed this question, and analyzed the intra- and intersegmental coupling between CPGs (i.e. the coupling between CPGs within one segment and the coupling between CPGs of different segments, respectively) in stick insects [12, 13] and locusts [14, 15]. In these works the authors studied the phase relations between rhythmic activities of *motoneuron* (MN) pools that drive the levator-depressor muscle pairs, which are responsible for the upward and downward motion of a leg. Using electrophysiological recordings of the rhythmic activities of the MNs, it was shown in [12] that the phase dynamics remarkably vary in different segments and change with respect to the presence or absence of the intersegmental coupling.

In this work we aim at finding the intra- and intersegmental coupling architecture of the CPG network involved in the control of the levator-depressor activities, using the results of [12]. For this purpose, we constructed a model of coupled phase oscillators by performing a phase reduction of the CPGs following [16, 17, 18, 19, 20, 21, 22]. Modeling of the interaction between body parts of an animal using the phase reduction approach has been applied in previous studies on locomotion in crayfish [23, 24], lamprey [25], and cockroach [26, 27]. Moreover, the analysis of phase relations was successfully used for the investigation of intersegmental couplings in lamprey [28], and in cockroach [29].

In our previous work [22] we performed a phase reduction of an escape type CPG [30, 31]. An escape type CPG has for instance been used to model the crustacean swimmeret system [32, 33, 21]. Moreover, this type of CPG is a core part of the stick insect walking model developed in the recent decade [34, 35, 36, 37, 38, 39, 40, 41, 42].

Results of our previous work [22] demonstrate that the phase reduction of the intersegmental network model of stick insect locomotion successfully reproduces the main properties of the original model. This was possible due to the fast threshold modulation property of the escape type CPG dynamics [43, 44, 45, 46].

In the current study we use the result of the phase reduction of the escape type CPG [22] and aim at finding possible coupling topologies and properties of the neural circuits that are able to reproduce the phase relations observed in the experiments in [12]. Therefore, we examined all possible coupling topologies of the neural circuit and found the ones that satisfied theoretically derived conditions and physiologically grounded restrictions.

The structure of this work is as follows: In the next section, we briefly explain the main aspects and the results of the experimental work in [12]. Then, in the theoretical part of this work we present the constructed model of coupled phase oscillators that describes the rhythmic activity of the levator-depressor MN pools in a general form as well as specifically for the escape type CPGs. Next, by analyzing the stability of this model we derive conditions that should be fulfilled by the coupling between CPGs in order to promote the phase relations observed in the experiments. Further, in the next section, we explain in detail the methods we use to analyze different neural circuit topologies. In Section 3, we present the results of the analysis and define possible coupling topologies of the CPG network. Further, in the same section, we generalize the results by approximating the coupling functions between the phase oscillators. Finally, we find general properties of the coupling in the CPG network for an arbitrary type of CPG.

2 Methods

2.1 Overview of the experimental results

The experiments reported in [12] were performed on stick insects of the species *Carausius morosus*. The activity of the motoneuron (MN) pools that activate the antagonistic levator-depressor trochanteris muscles, which perform the upward and downward movement of the legs, was recorded and analyzed. For this purpose, the authors focused their study on the coxa-trochanter (CTr) joint of the insect, for which in every hemisegment the levator and depressor throchanteris MN pools are present, and each of these pools consists of only two excitatory motoneurons (a slow and a fast motoneuron (MN)). In the experimental setup, the neural circuits in a segment (ganglion), including CPG networks and MN pools, were activated chemically using pilocarpine, which elicits an alternating rhythmic activity of the levator-depressor MN pools, as it was shown in [11, 47, 48].

The electrophysiological measurements were conducted using hook electrodes placed on the lateral nerve C2 of the nervus cruris [49, 4]. This nerve carries the axons that activate the depressor trochanteris muscle [50, 51]. The experiments were performed in the meso-, meta- and prothoracic ganglia. In this work we concentrate on the results of [12] that relate only to the analysis of the meso- and metathoracic ganglia, i.e. we do not consider the results related to the analysis of the prothoracic ganglion.

Four different sets of experiments were performed. In Fig. 1 we present a scheme that reflects these experiments and their results. In the first two sets of experiments, the electrophysiological recordings were done in isolated meso- and metathoracic ganglia, as shown in Fig. 1A. The results of these experiments demonstrated that when the mesothoracic ganglion was activated by pilocarpine, the contralateral depressor MNs establish in-phase rhythmic activity. Whereas, when the same experiment was performed in the metathoracic ganglion, the contralateral MNs show anti-phase rhythmic activity.

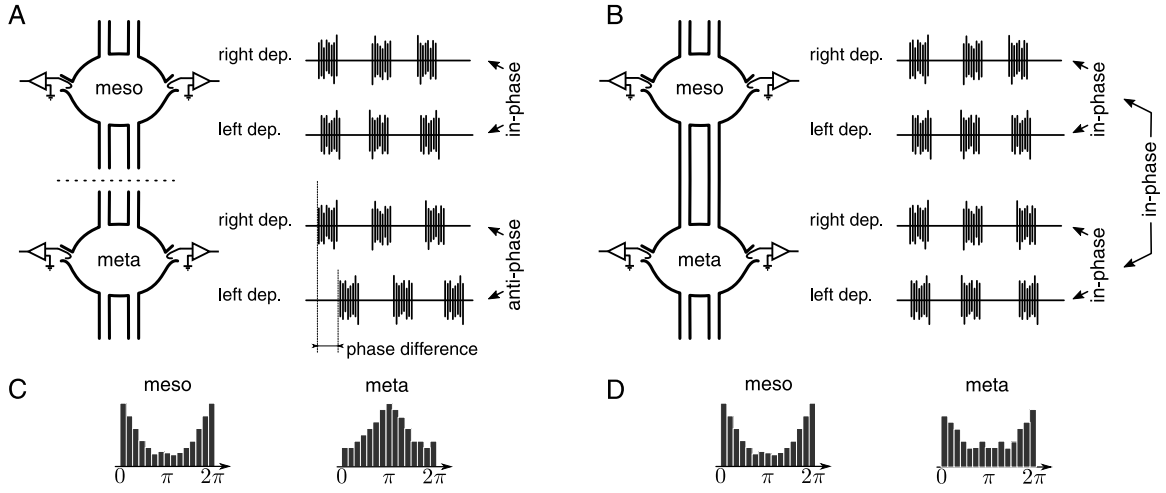

Figure 1: Schematic representation of the results of [12]. Only the results related to the meso- and metathoracic ganglia are shown. A: Scheme of the experiments, where isolated segments were analyzed. B: Scheme of the experiments, where interconnected segments were analyzed. In both cases the segments were activated chemically, and electrophysiological recordings of the left and right depressor motoneuron (MN) pools were performed using hook electrodes (denoted as amplifiers with hooks). The corresponding extracellular recordings are presented as periodic spike bursts on the right hand side of the schemes. The zero phase of the oscillatory activity was associated with the beginning of the spike bursts (panel A, right bottom). Then the phase differences between the activities of the contralateral MNs were plotted as histograms. C: The histogram of the phase differences in the case of isolated segments (shown in panel A). In-phase and anti-phase synchrony between the oscillatory activities of the contralateral depressor MNs were observed in the isolated meso- and metathoracic ganglia, respectively. D: The phase difference histograms in the case of interconnected segments (shown in panel B). In both ganglia the oscillatory activities of the contralateral depressor MNs demonstrate overall in-phase synchrony.

As a quantitative evidence, an analysis of the phase difference between the rhythmic activities of the contralateral MNs was performed. For this purpose, the beginning of one burst of depressor MN activity was defined as zero phase and the beginning of the subsequent burst as one period, i.e. a phase increase of 2π (see Fig. 1A). Between two bursts the phase was linearly approximated. Further, a histogram of all observed phases was plotted and analyzed (Fig. 1C). This analysis showed that the distribution of the phase differences between the activities of the contralateral depressor MNs in the mesothoracic ganglion was on average around zero (or 2π), whereas the one in the metathoracic ganglion was around π (Fig. 1C).

In the third set of experiments the connections between the meso- and metathoracic ganglia were present (Fig. 1B) and both segments were activated by pilocarpine. In this case, the activities of the depressor MNs in both ganglia were oscillating in-phase. The maximum of the distribution of the phase differences of the contralateral depressor MNs in both ganglia were around zero, as shown in Fig. 1D.

In Fig. 1B we depicted the ipsilateral depressor MN activities as being in-phase (between segments). This was not quantitatively analyzed in [12]. However, from personal communication with Mantziaris and colleagues, and from the time courses of the electrophysiological measurements presented in [12], we conclude that when the meso- and the metathoracic ganglia are interconnected the activities of not only the contralateral, but also of the ipsilateral depressor MNs are in-phase. In-phase activity of the ipsilateral depressor MNs was also observed in experimental works [14, 15] on locusts (a close relative of the stick insect).

In the fourth set of experiments, the phase difference of the activity of contralateral depressor MNs in the metathoracic ganglion was analyzed before and after chemical activation of the interconnected mesothoracic ganglion. This case is not shown in Fig. 1. The results of these experiments demonstrated that, before activation of the mesothoracic ganglion with pilocarpine, the bursting in the metathoracic ganglion revealed no rhythmic oscillatory pattern and had no preferred phase difference. However, after activation of the mesothoracic ganglion, the activity of the contralateral depressor MNs in the metathoracic ganglion changed to in-phase oscillatory activity, similar to the activity observed in the third set of experiments (Fig. 1B and D), with a mean phase difference around zero. Thus, these results demonstrate a weak in-phase coupling of the oscillatory activity of the depressor MNs of both segments due to descending intersegmental neural signals from the meso- to the metathoracic ganglion.

According to these results, we conclude that in an isolated mesothoracic ganglion after chemical activation the contralateral depressor MNs tend to display in-phase oscillatory activity. Whereas, in an isolated and chemically activated metathoracic ganglion these oscillatory activities have the tendency to be in anti-phase. Moreover, when the two segments are interconnected, the oscillatory activity of the contralateral and ipsilateral depressor MNs are overall in-phase. We can also conclude that a descending intersegmental connection from the meso- to the metathoracic ganglion elicits these in-phase oscillatory activities in both ganglia. Taking into account these results of [12] we built a theoretical model of coupled phase oscillators in the next section.

2.2 Theory

2.2.1 Phase reduction approach

In this work we use a model of coupled phase oscillators to examine the properties of the interaction between neural circuits that drive the levator-depressor muscle pairs. The scheme of the neural circuit of one segment is shown in Fig. 2A. Every CPG consists of two mutually inhibitory interneurons (dashed rectangles). The model of the neural circuit shown in Fig. 2A is based on the results of the experimental studies [52, 53], which found that the CPGs are not directly connected to the MNs, but via nonspiking interneurons (INs). Whenever a CPG interneuron is active, it excites an IN that inhibits the corresponding MN (Fig 2A). Therefore, we can associate the activity of the CPG interneurons with the activity of the levator or depressor MNs. In Fig. 2A the CPG interneuron that is associated with the depressor MN activity is marked with a red circle and labeled as dep; the blue circle labeled as lev is the one associated with the levator MN activity. The activities of the depressor MNs were measured in the experiments.

Coupled phase oscillator models is a widely used mathematical framework to study the dynamics of interconnected oscillatory systems. Within this framework the state of an oscillator is defined by a scalar variable, i.e. by its phase φ. Without any external input the phase of an oscillatory system grows monotonically $\dot{\varphi} = \omega$. In the presence of an input to the system its phase grows faster or slower

depending on the magnitude of the input (the coupling strength), which changes with respect to the state of both systems involved in the coupling. Particularly, if an oscillator j drives an oscillator k then the phase dynamics for the latter reads

$$\dot{\varphi}_k = \omega_k + H(\varphi_j - \varphi_k), \tag{1}$$

where $H(\varphi_j - \varphi_k)$ is the phase interaction function or *the coupling function*. By analyzing the properties of the coupling function we analyze the properties of the interaction (coupling) between the neural circuits.

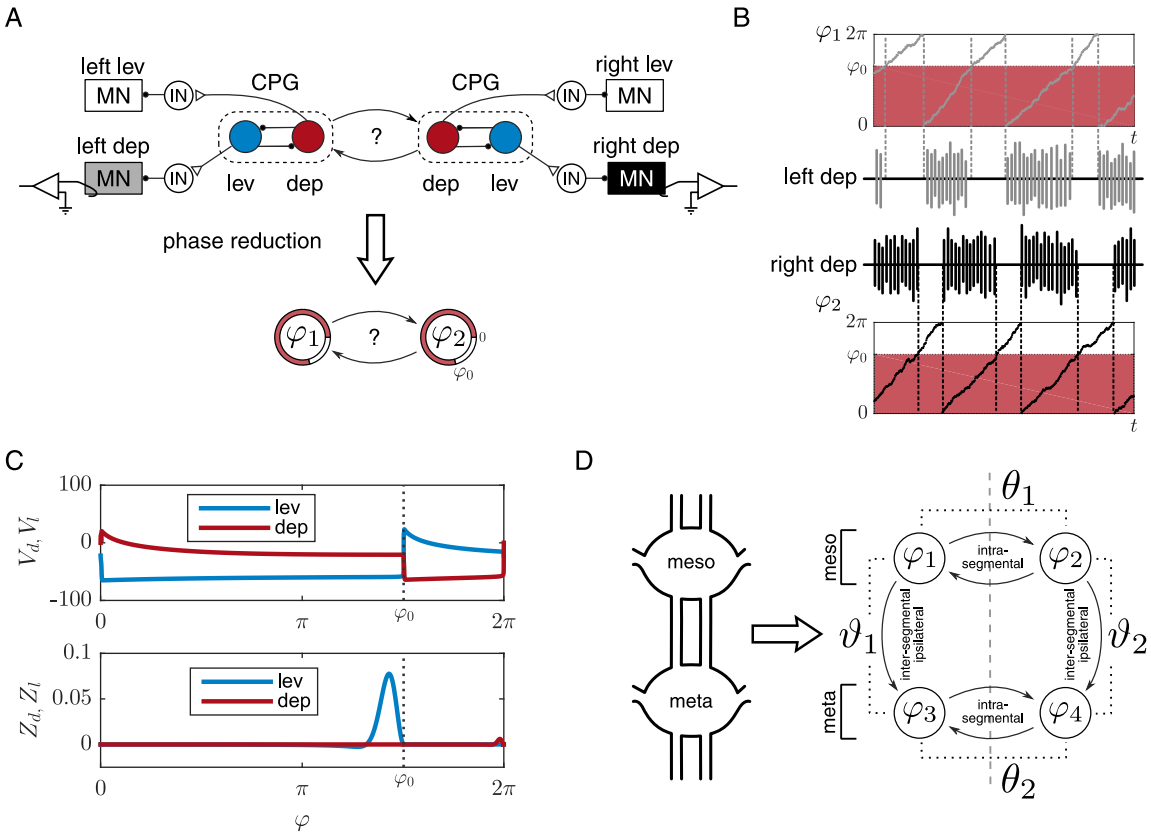

Figure 2: Phase reduction of the neural circuits that control the contralateral levator-depressor muscle pairs. A: Scheme of the neural circuits in one segment. Levator (lev) and depressor (dep) motoneurons (MN, shown as solid rectangles) are connected to the CPGs (dashed rectangles) via inhibitory interneurons (IN, circles). The latter are activated by the interneurons of the CPG: the levator (blue circles) and the depressor interneurons (red circles). In the experiments, the activity of the left and right depressor motoneurons are measured (denoted by grey and black rectangles, and symbols of amplifiers with hook electrodes). We reduce the neural circuit of one segment to a model of two coupled phase oscillators with the phases φ_1 and φ_2. B: Association of the activity of the depressor motoneurons with the phase of the oscillators: the depressor MNs are active when the phase φ_i of the corresponding phase oscillator i is within the range $(0, \varphi_0)$ (red area), where φ_0 is the duty factor. This association is also shown in panel A bottom as red and white borders of the phase oscillator circles. C: An example of the membrane potential V and the infinitesimal phase response curve (iPRC) Z for an escape type CPG calculated in [22]. More detailed information on the iPRC is presented in A. The activity of the levator (lev, blue curves) and depressor (dep, red curves) interneurons of a CPG switches at 0 or at φ_0 phase. D: The phase reduced model of the neural circuit that controls the levator-depressor MN activities in the meso- and metathoracic ganglia. Vertical dashed line shows the left-right symmetry axis. The phase differences $(\theta_1,\theta_2,\vartheta_1,\vartheta_2)$ are denoted by dotted lines.

To perform the phase reduction of the neural system that activates the levator-depressor MNs and

muscles we make several assumptions. We assume that chemically activated CPGs oscillate in a stochastic manner [11], and their phase does not grow linearly, as it is shown in Fig. 2B. Therefore, there could be spontaneous switching between activities of the levator and depressor MNs. However, due to mutual inhibition between the CPG interneurons these activities appear to be alternating. On the other hand, if CPGs are connected to each other, then this interaction will adjust the activities of the CPGs in time. This means that the phase differences between the activities of the CPGs will tend to a certain value which is defined by the properties of the coupling between the CPGs. Therefore, in the experiments, the phase differences on average appear to be distributed around a certain maximum value. A similar assumption has been used to estimate the coupling strength within the CPG network of the lamprey spinal cord [54, 55].

We reduce every CPG, i.e. every pair of mutually inhibitory interneurons, to a phase oscillator. Similarly to [22] we directly relate the activity of a CPG phase oscillator to the activity of the corresponding MNs. That is, if the phase of the oscillator is within the range $(0, \varphi_0)$ then the depressor MN is active; and vice versa, for the phase values $(\varphi_0, 2\pi)$ the levator MN is active. This relation between the phases of the CPGs and the bursting activities of the MNs is demonstrated in Fig. 2B. We can define the switch from depressor being active to levator being active as the time when the phase value crosses the threshold value φ_0. It was shown in [22] that this assumption works very well for an escape type CPG. In the same manner, as it was done in the analysis of the experimental data in [12], in our analysis the zero phase is defined as the beginning of the depressor MN bursting activity, i.e. that of the depressor CPG interneuron.

Next, we demonstrate how to derive the phase equation Eq. (1) for a CPG following [16, 17, 18, 19, 20]. Let us consider a system $\dot{\mathbf{x}} = \mathbf{f}(\mathbf{x})$ which has an attractive hyperbolic limit cycle Γ_0 and oscillates with a period T. If the oscillator is subject to a weak external input $\mathbf{g}$

$$\dot{\mathbf{x}} = \mathbf{f}(\mathbf{x}) + \epsilon \mathbf{g}(\mathbf{x}, t), x \in \mathbb{R}^{n+1}, \quad 0 < \epsilon \ll 1, \tag{2}$$

then it can be reduced to a phase oscillator of the following form

$$\dot{\varphi} = \omega_0 + \epsilon \sum_n \frac{\partial \varphi}{\partial x_n}\big(x_0(\varphi)\big) \mathrm{g}_n\big(\mathbf{x_0}(\varphi), t\big)\Big|_{\mathbf{x_0} \in \Gamma_0}, \tag{3}$$

where $\omega_0 = 2\pi/T$, φ is the phase of the oscillator in a neighborhood of Γ_0, and $\frac{\partial \varphi}{\partial x_n}$ is the n^{th} component of the infinitesimal phase response curve (iPRC) [20, 19, 16]. Further in the text we will denote iPRC by Z.

If a CPG k receives a direct synaptic input from a CPG j then the synaptic input current is

$$I_{kj} = g_{syn,k} s\big(V_j\big)\big(V_k - E_0\big),$$

where $g_{syn,k}$ is the synaptic conductance, E_0 is the reversal potential, V_k and V_j are the membrane potentials of the interneurons of the CPGs k and j, and s is the synaptic activation function. Due to fast synaptic transition we set $s = s_\infty$,

$$s_\infty(V) = \frac{1}{1 + \exp\big(\gamma_s(V - V_{hs})\big)}. \tag{4}$$

The phase-reduced equation for the CPG k can be written as

$$\dot{\varphi}_k = \omega_0 - \frac{1}{C_m} Z_k(V_k(\varphi_k)) I_{kj}(V_k(\varphi_k), V_j(\varphi_j)) = \omega_0 - c_{kj} Z_k(V_k(\varphi_k))\big(V_k(\varphi_k) - E_0\big) s_\infty\big(V_j(\varphi_j)\big), \tag{5}$$

where $c_{kj} = g_{syn,k}/C_m$. Here, and further in the text, we assume that all CPGs have the same oscillation frequency ω_0.

The averaged phase equation of Eq. (5) can be derived by introducing a phase deviation $\psi = \varphi - \omega_0 t$ into Eq. (5) and averaging it over the period T [18, 20, 19, 22]:

$$\dot{\psi}_k = -\frac{c_{kj}}{T} \int_0^T Z_k(\psi_k + \omega_0 t)(V_k(\psi_k + \omega_0 t) - E_0) s_\infty(V_j(\psi_j + \omega_0 t)) \mathrm{d}t. \tag{6}$$

Let us define a new time variable $\tau = \psi_k + \omega_0 t$. Then using the relation $\psi_j + \omega_0 t = \psi_j - \psi_k + \tau$ we can write

$$\dot{\psi}_k = H_{kj}(\psi_j - \psi_k), \tag{7}$$

where

$$H_{kj}(\theta) = -\frac{c_{kj}}{2\pi}\int_0^{2\pi} Z_k(\tau)(V_k(\tau) - E_0)s_\infty(V_j(\theta+\tau))\mathrm{d}\tau. \tag{8}$$

We obtain Eq. (1) from Eq. (7) by using the phase deviation $\psi = \varphi - \omega_0 t$.

In this work we built a model of coupled phase oscillators with the assumption that all CPGs that control the levator-depressor muscle pairs in the meso- and metathoracic ganglia are identical, and the variety of the properties of these CPGs observed in the experiments are caused by the different topologies of the inter-CPG couplings. Therefore, we use the same phase oscillator model for all CPGs. In other words, we assume that the iPRCs and the membrane potentials of all CPGs are equal. Further in the text, we use the lower indices d and l to denote the specific component of the CPG. Namely, we denote by Z_l and Z_d the components of the iPRC, and by V_d and V_l the components of the membrane potentials that correspond to the levator and depressor interneurons of the CPG, respectively. Examples of the membrane potentials and iPRCs for an escape type CPG calculated in [22] are shown in Fig. 2C. The properties of the iPRC for an escape type CPG are discussed in detail in A.

The phase dynamic equation written in the form of Eq. (1) does not specify the connection between the CPGs. Therefore, Eq. (1) is generic and can be applied to any type of coupling between CPGs. In order to distinguish a specific type of coupling we introduce the following notation: we use the letter l for denoting levator, d for depressor; i and e to denote inhibitory and excitatory synaptic connections. Also the coupling function of a specific coupling type is denoted with lower indices of the from-to-type format, which is a combination of the letters l, d, i and e. For example, if the *levator* interneuron of a CPG k receives an *excitatory* synaptic connection from the *depressor* interneuron of a CPG j then the coupling function in the phase equation of the phase oscillator k is defined as

$$H_{dle}(\varphi_j - \varphi_k) = -\frac{c_{kj}}{2\pi}\int_0^{2\pi} Z_l(\tau)\,(V_l(\tau) - E_0^e)\,s_\infty(V_d(\varphi_j - \varphi_k + \tau))\mathrm{d}\tau. \tag{9}$$

In other words, the lower indices *dle* denote the excitatory type synaptic coupling from the depressor to the levator interneuron of the CPGs.

2.2.2 Coupled phase oscillators model

In this section we reduce the system of CPGs that drive the levator-depressor muscle pairs in the meso- and metathoracic ganglia to a system of four coupled phase oscillators as it is shown in Fig. 2D. In the model the connections between the CPGs are constructed by taking into account a lateral symmetry [1]. We refer to the connections within a segment as intrasegmental. They can be different for the meso- and metathoracic segments. However, due to the lateral symmetry the contralateral connections within a segment (from left to right and from right to left) are the same. Similarly, the connections between segments, i.e. the intersegmental connections are laterally symmetric. According to the results of the previous studies [56, 47, 48] and the results of the fourth set of experiments in [12], previously described in Section 2.1, we consider only ipsilateral intersegmental descending connections from the meso- to metathoracic ganglion (Fig. 2D).

We built a model of coupled phase oscillators in a general form using the averaged coupling functions (Eq. (8)), without explicitly defining the type of synaptic connection. Therefore, we use lower indices *ms*, *mt*, and *ip* to denote the intrasegmental contralateral connections within the *meso-* and *meta*-thoracic ganglia, and the intersegmental *ipsilateral* connections between ganglia, respectively.

Thus, the system of phase equations reads

$$\dot{\varphi}_1 = \omega_0 + c_{ms}H_{ms}(\varphi_2 - \varphi_1), \tag{10}$$
$$\dot{\varphi}_2 = \omega_0 + c_{ms}H_{ms}(\varphi_1 - \varphi_2), \tag{11}$$
$$\dot{\varphi}_3 = \omega_0 + c_{mt}H_{mt}(\varphi_4 - \varphi_3) + c_{ip}H_{ip}(\varphi_1 - \varphi_3), \tag{12}$$
$$\dot{\varphi}_4 = \omega_0 + c_{mt}H_{mt}(\varphi_3 - \varphi_4) + c_{ip}H_{ip}(\varphi_2 - \varphi_4), \tag{13}$$

where c_{mt}, c_{ms}, c_{ip} denote the specific connection strengths. It needs to be mentioned here that the connection strengths can not be negative. We introduce the following phase differences, as it is shown in Fig. 2D:

$$\begin{aligned}\theta_1 &= \varphi_1 - \varphi_2,\\ \theta_2 &= \varphi_3 - \varphi_4,\\ \vartheta_1 &= \varphi_1 - \varphi_3,\\ \vartheta_2 &= \varphi_2 - \varphi_4.\end{aligned} \tag{14}$$

There is an obvious relation between these phase variables:

$$\theta_1 - \theta_2 = \vartheta_1 - \vartheta_2. \tag{15}$$

Then, by subtracting Eqs. (11) and (12) from Eq. (10), and Eq. (13) from Eqs. (11) and (12) we obtain a system of equations for the phase differences

$$\dot{\theta}_1 = c_{ms}H_{ms}(-\theta_1) - c_{ms}H_{ms}(\theta_1), \tag{16}$$

$$\dot{\theta}_2 = c_{mt}H_{mt}(-\theta_2) - c_{mt}H_{mt}(\theta_2) + c_{ip}H_{ip}(\vartheta_1) - c_{ip}H_{ip}(\vartheta_2), \tag{17}$$

$$\dot{\vartheta}_1 = c_{ms}H_{ms}(-\theta_1) - c_{mt}H_{mt}(-\theta_2) - c_{ip}H_{ip}(\vartheta_1), \tag{18}$$

$$\dot{\vartheta}_2 = c_{ms}H_{ms}(\theta_1) - c_{mt}H_{mt}(\theta_2) - c_{ip}H_{ip}(\vartheta_2). \tag{19}$$

2.2.3 Analysis of the intrasegmental couplings

As discussed in Section 2.1, the results of the study [12] show that in the mesothoracic ganglion the distribution of the phase differences between contralateral CPGs, which control the levator-depressor MN activities, have a maximum around zero. In contrast, in the metathoracic ganglion the distribution of the phase differences between contralateral CPGs has its maximum around π. In this chapter we analyze the properties of the H functions of the contralateral couplings that result in the phase difference distributions observed in the experiments.

Let us consider the case when the segments are isolated (Fig. 1A), i.e. we analyze the solutions of Eqs. (16) and (17) under the condition $c_{ip} = 0$:

$$\dot{\theta}_1 = c_{ms}H_{ms}(-\theta_1) - c_{ms}H_{ms}(\theta_1), \tag{20}$$

$$\dot{\theta}_2 = c_{mt}H_{mt}(-\theta_2) - c_{mt}H_{mt}(\theta_2), \tag{21}$$

These equations are similar and the right hand side of these equations are 2π-periodic even functions of the following form:

$$G(\theta) = H(-\theta) - H(\theta). \tag{22}$$

Therefore, irrespective of the H functions the function G has zeros at $\theta = 0$ (or $\theta = 2\pi$) and $\theta = \pi$. Moreover, if $G(\theta^*) = 0$ then $G(2\pi - \theta^*) = 0$.

The fixed points of Eqs. (20) and (21) are stable, if the derivatives of the function G are negative at the fixed points. However, as demonstrated in Fig. 3 the stability of the fixed points can not exclusively define the distribution of the phase difference θ.

Obviously, when the function G has zeros only at 0 (or 2π) and at π, the distribution centers around the stable fixed point as shown in Fig. 3A and B: if $\theta = 0$ is stable then the solution of the stochastic Eqs. (20) or (21) is in-phase (Fig. 3A); on contrary, if $\theta = \pi$ is stable then the solution is anti-phase (Fig. 3B). On the other hand, if the function G in addition has two zeros at θ^* and $2\pi - \theta^*$, then the distribution of the phase differences depends on the value and the stability of these fixed points (Fig. 3C and D). Indeed, if θ^* is closer to π than to 0, as shown in Fig. 3C, then in the case of unstable fixed points at θ^* and $2\pi - \theta^*$, the resulting distribution of the phase differences appears to be centered around 0. Conversely, for stable fixed points at θ^* and $2\pi - \theta^*$, as shown in Fig. 3D, the resulting distribution, which is the sum of the two distributions around the stable fixed points, is centered around π. When θ^* is closer to 0 than to π then the resulting distribution is quite opposite: it is centered around π if the fixed points at θ^* and $2\pi - \theta^*$ are unstable, and is centered around 0 if the fixed points at θ^* and

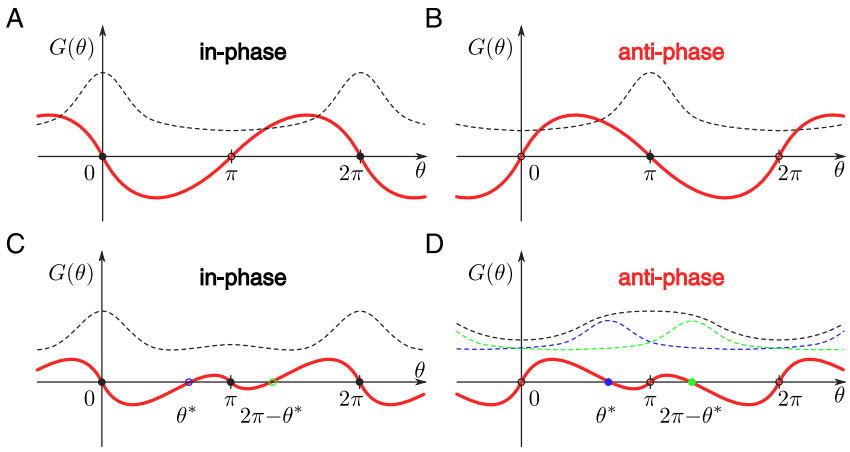

Figure 3: Examples of the function $G(\theta)$, its zeros and the corresponding distribution of the phase difference θ. The filled and unfilled circles denote the zeros that correspond to the stable and unstable fixed points of Eqs. (20) and (21), respectively. Dashed lines represent the distribution of the phase difference θ, when Eqs. (20) and (21) are stochastic. A: The function G has zeros only at 0 (or 2π, stable fixed point) and at π (unstable fixed point). The distribution centers around 0, which corresponds to the in-phase solution of Eqs. (20) and (21). B: Similar to A, but with a stable fixed point at π and an unstable one at 0 (or 2π). The distribution centers around π, i.e. the anti-phase solution. C: The function G has 4 zeros: stable fixed points at 0 (or 2π) and π, and unstable ones at θ^* (unfilled blue circle) and $2\pi - \theta^*$ (unfilled green circle). Since θ^* is closer to π the distribution of the phase difference appears to be centered around 0, and the solution of Eqs. (20) and (21) is in-phase. D: Similar to C, but with unstable fixed points at 0 (or 2π) and π, and stable ones at θ^* (filled blue circle) and $2\pi - \theta^*$ (filled green circle). In this case, the resulting distribution (dashed black line), which can be represented as the sum of two separate distributions around stable fixed points (dashed blue and green lines), is effectively centered around π, thereby resulting in the anti-phase solution of Eqs. (20) and (21).

$2\pi - \theta^*$ are stable. In case of more fixed points the distribution of the phase differences would not have any distinguishable peaks and will approach uniform distribution.

In summary, to identify whether a specific coupling induces in-phase or anti-phase activities of the contralateral depressor MNs we analyze the fixed points of Eqs. (20) and (21). If there are only two fixed points at 0 (or 2π) and π then the stability of these fixed points define the contralateral activities to be in-phase or in anti-phase, as shown in Figs. 3A and B: the in-phase activity if

$$\frac{\partial G}{\partial \theta}(0) < 0 \text{ and } \frac{\partial G}{\partial \theta}(\pi) > 0, \text{ thus, } \frac{\partial H}{\partial \theta}(0) > 0 \text{ and } \frac{\partial H}{\partial \theta}(\pi) < 0, \tag{23}$$

and the anti-phase activity if

$$\frac{\partial G}{\partial \theta}(0) > 0 \text{ and } \frac{\partial G}{\partial \theta}(\pi) < 0, \text{ thus, } \frac{\partial H}{\partial \theta}(0) < 0 \text{ and } \frac{\partial H}{\partial \theta}(\pi) > 0. \tag{24}$$

However, in the cases with more than two fixed points, as shown in Figs. 3C and D, not only the stability of the fixed points, but also their distribution should be taken into account.

2.2.4 Analysis of the intersegmental couplings

In this section we derive conditions for the intersegmental couplings. For this purpose, we analyze the solutions of Eqs. (16), (18) and (19) together with $c_{ip} \neq 0$. We don't need to consider Eq. (17), since it can be derived from Eqs. (16), (18) and (19), taking into account the relation between the phase differences Eq. (15).

Let us rewrite Eqs. (16), (18) and (19) using Eq. (15) as follows:

$$\dot{\theta}_1 = c_{ms}H_{ms}(-\theta_1) - c_{ms}H_{ms}(\theta_1),$$
$$\dot{\vartheta}_1 = c_{ms}H_{ms}(-\theta_1) - c_{mt}H_{mt}(-\theta_1 + \vartheta_1 - \vartheta_2) - c_{ip}H_{ip}(\vartheta_1),$$
$$\dot{\vartheta}_2 = c_{ms}H_{ms}(\theta_1) - c_{mt}H_{mt}(\theta_1 - \vartheta_1 + \vartheta_2) - c_{ip}H_{ip}(\vartheta_2).$$

Then we divide the system by c_{mt} and redefine the time variable $t = c_{mt}t$. By introducing new variables $\mu = c_{ms}/c_{mt}$ and $\rho = c_{ip}/c_{mt}$ the system reads

$$\dot{\theta}_1 = f_0(\theta_1) = \mu H_{ms}(-\theta_1) - \mu H_{ms}(\theta_1), \tag{25}$$
$$\dot{\vartheta}_1 = f_1(\theta_1, \vartheta_1, \vartheta_2) = \mu H_{ms}(-\theta_1) - H_{mt}(-\theta_1 + \vartheta_1 - \vartheta_2) - \rho H_{ip}(\vartheta_1), \tag{26}$$
$$\dot{\vartheta}_2 = f_2(\theta_1, \vartheta_1, \vartheta_2) = \mu H_{ms}(\theta_1) - H_{mt}(\theta_1 - \vartheta_1 + \vartheta_2) - \rho H_{ip}(\vartheta_2). \tag{27}$$

The results of the experiments show that with interconnected meso- and metathoracic ganglia the contralateral, i.e. the left and right depressor MNs in these ganglia express in-phase activity (Fig. 1B and D). Thus, $\theta_1 = 0$, $\theta_2 = 0$. As we discussed in Section 2.1, the activities of the ipsilateral depressor MNs (between ganglia) are also in-phase. Therefore, according to Eq. (15) we search for a solution $\vartheta_1 = \vartheta_2 = 0$.

The system Eqs. (25), (26) and (27) has a zero solution $(\theta_1, \vartheta_1, \vartheta_2) = (0, 0, 0)$ if Eq. (25) has a zero solution (which is always the case) and if

$$\mu H_{ms}(0) = H_{mt}(0) + \rho H_{ip}(0). \tag{28}$$

The stability analysis of Eqs. (25), (26) and (27) reveals that the system has no foci (see B), and that the zero solution is stable if the following conditions are fulfilled

$$\frac{\partial H_{ms}}{\partial \theta}(0) > 0, \tag{29}$$

$$\frac{\partial H_{ip}}{\partial \theta}(0) > 0, \tag{30}$$

$$\rho > \rho_{\min} = -2\frac{\partial H_{mt}}{\partial \theta}(0) / \frac{\partial H_{ip}}{\partial \theta}(0). \tag{31}$$

The conditions Eqs. (29) and (30) can be interpreted in the way that the intrasegmental couplings in the mesothoracic ganglion and the intersegmental ipsilateral couplings should induce stable in-phase activity. Moreover, the condition Eq. (31) implies that the strength of the intersegmental ipsilateral coupling should be stronger than the intrasegmental contralateral one in the metathoracic ganglion, and their ratio, i.e. the parameter ρ, should be larger than a specific value ($\rho_{\min}$). In other words, the in-phase ipsilateral coupling should overplay the anti-phase contralateral coupling in the metathoracic ganglion.

2.3 Method of analysis

In the previous section we performed a phase reduction of the CPGs in a general form, i.e. without explicitly specifying the coupling types and the topology of the network. In this section we introduce the methods of analysis of the system for specific synaptic connection types using the results of the theoretical analysis from the previous section.

First, we explain what kind of synaptic coupling types and connection topologies were considered in the analysis. Next, we describe how the analysis of different coupling types and topologies using the conditions on the parameters of the system derived in the previous section was performed.

2.3.1 Network topologies

In this work we consider only chemical synapses between CPGs, namely, excitatory and inhibitory synaptic connections. As it was mentioned in Section 2.2.1, in our model the CPG has two interneurons that control the activity of the levator and depressor muscle pairs, which we refer to as the levator and the

depressor interneurons of the CPG, respectively. Let us consider a synaptic coupling between two CPGs. The synapse can either originate from the levator or from the depressor interneuron of the presynaptic CPG. Similarly, the synaptic coupling can end either on the levator or the depressor interneuron of the postsynaptic CPG. Therefore, we have $2 \times 2 \times 2 = 8$ different types of couplings. Again, we will denote these 8 synaptic couplings with a three letter notation of the *from-to-type* form, similar to the lower indices in Eq. (9). All 8 different intrasegmental contralateral synaptic couplings are shown in Fig. 4A. Here we assume that, within a segment, there is only one type of symmetric contralateral connection between CPGs. The intersegmental ipsilateral synaptic couplings are shown in Fig. 4B, where only one side is depicted; the contralateral side is identical. Further in the text, we refer to the coupling configurations shown in Fig. 4 as *coupling types*. One important thing to be noticed here is that due to the contralateral symmetry every coupling type has two identical synaptic couplings: (i) two symmetric contralateral synaptic couplings within a segment and (ii) two symmetric ipsilateral synaptic couplings between segments. We label the coupling types also with the three letter notation put in parentheses. For example, the notation (dle) denotes a coupling type with two symmetric excitatory synaptic couplings, which start at the depressor interneurons of the CPGs and end at the levator interneurons of the CPGs.

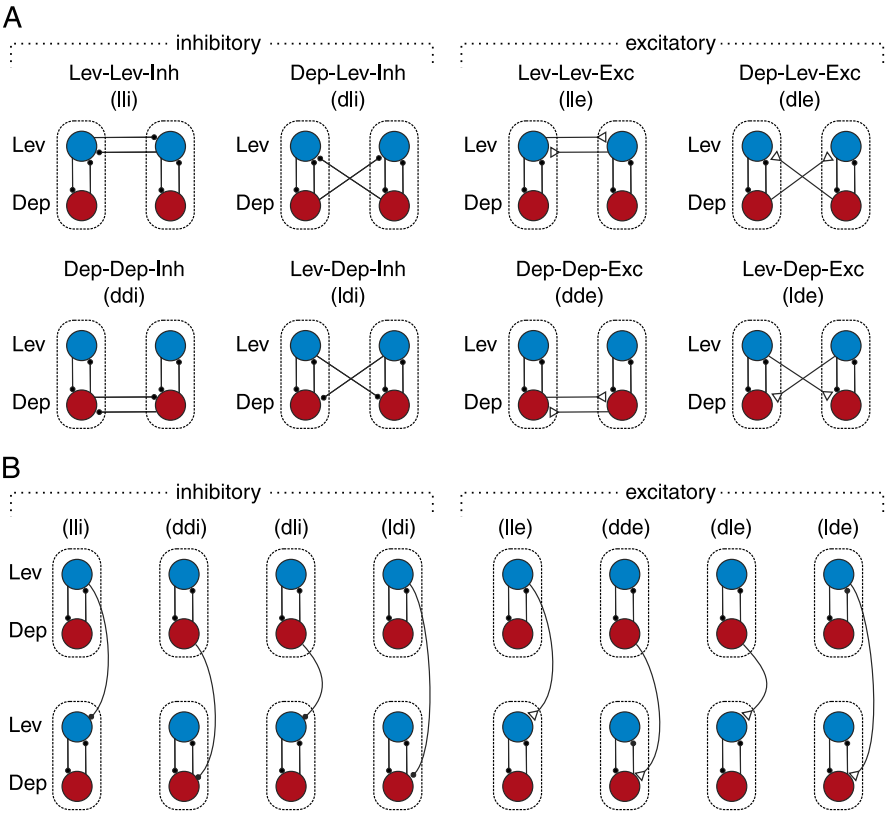

Figure 4: Types of intra- and intersegmental synaptic couplings. A: Types of intrasegmental synaptic couplings: every case consists of two similar contralateral synaptic connections. B: types of intersegmental ipsilateral synaptic couplings. Only one side is shown. The contralateral side is identical. The CPGs are denoted by two mutually inhibitory interneurons surrounded by dashed rectangles. The levator and depressor interneurons of the CPGs, are shown as in Fig. 2 as blue and red circles, respectively.

Since we have 8 possible intrasegmental coupling combinations in the meso- and metathoracic segments, and 8 possible intersegmental coupling combinations, we consider, in total, for the whole system $8 \times 8 \times 8 = 512$ different possible network topologies. Further we use the (*meso*)-(*meta*)-(*ipsi*) notation to denote different *coupling combinations* (or *network topologies*). Namely, in the notation, instead of *meso* and *meta* we write the specific coupling type of the intrasegmental coupling in the meso- and metathoracic segments, and instead of *ipsi* the specific coupling type of the intersegmental ipsilateral couplings.

For example, the notation (lli)-(dle)-(lde) means that the two symmetric contralateral synaptic couplings in the mesothoracic ganglion are of the (lli) type, the ones in the metathoracic ganglion are of the (dle) type, and the two symmetric intersegmental ipsilateral synaptic couplings are of the (lde) type.

In the next section we present the methods of analysis of the coupling types that let us exclude some combinations as being less possible.

2.3.2 Analysis of the stability

The conditions previously derived in Section 2.2 can be categorized into two groups: the conditions for the coupling functions (Eqs. (23), (24), (29), and (30)), and the conditions for the parameters μ and ρ (Eqs. (28) and (31)).

First, we analyze the coupling functions for different coupling types separately. For this purpose, we calculate the coupling functions H for all coupling types shown in Fig. 4 using the iPRC Z and the membrane potential V found in [22] for an escape type CPG (see Fig. 2C and A). It needs to be mentioned here, that, as we assumed previously, all CPGs are similar and are directly coupled to each other via chemical synapses. Therefore, despite of being either an intra- or intersegmental coupling, a specific coupling function H is defined only by its coupling type (see Eq. (9)), denoted by the (*from-to-type*) notation. Hence, we analyze only 8 types of coupling functions H, for the coupling types shown in Fig. 4A or B.

Further, we test the stability and the distribution of the fixed points of the coupling functions as discussed in Section 2.2.3 to determine which coupling types are possible for the intrasegmental and the intersegmental connections within and between the meso- and the metathoracic ganglia. This reduces the overall number of the combinations to analyze.

Next, after defining possible combinations (network topologies), we analyze the whole network (a combination of different H_{ms}, H_{mt}, H_{ip}) using Eq. (28). This equation defines the linear relation between the parameters μ and ρ necessary to induce the in-phase activity of the depressor MNs, when the meso- and the metathoracic ganglia are connected. An example of this linear relation is shown in Fig. 5A.

The parameter μ defines the ratio of the strengths of the intrasegmental coupling in the mesothoracic ganglion to the one in the metathoracic ganglion. The parameter ρ, however, defines the ratio of the intersegmental ipsilateral connection to the intrasegmental coupling in the metathoracic ganglion. Thus, they are positive quantities: $\mu > 0$ and $\rho > 0$. Due to physiological reasons we assume that the strengths of the considered couplings can not differ more than ten times. Therefore, we set limiting conditions for these parameters and consider the solutions only for the coupling combinations that satisfy the following conditions

$$1/10 < \mu < 10 \text{ and } 1/10 < \rho < 10. \tag{32}$$

These conditions represent an area, shown in Fig. 5A, with vertical and horizontal dashed-line borders.

The relation between the activity of the depressor MNs (i.e. being in-phase or in anti-phase) was observed in the experiments for all animals, which indicates that this is an important property of the couplings between the CPGs of the same and neighboring segments to perform coordinated stepping. The coupling strengths c_{ms}, c_{mt} and c_{ip}, and respectively the values of the parameters μ and ρ, could of course be different between animals but their distribution must lie within a specific physiological range. Moreover, if the strength of a coupling is changed in an animal (e.g. due to environmental or developmental influences) then the strengths of the other couplings should change correspondingly to maintain the phase relation between the MNs. Very steep or flat $\mu(\rho)$ lines are therefore physiologically unreasonable: a small change of the strength of a particular coupling requires a comparably tremendous change of the strength of other couplings to be able to maintain the phase relation. Therefore, in our analysis we exclude coupling combinations with steep or flat $\mu(\rho)$ lines.

As the theoretical analysis shows, the solution $(\theta_1, \vartheta_1, \vartheta_2) = (0, 0, 0)$ is stable if the conditions Eqs. (29), (30), and (31) are fulfilled. The latter condition is shown in Fig. 5A as a vertical dotted line. With respect to the conditions Eq. (32) we exclude in our analysis the combinations of H_{ms}, H_{mt}, H_{ip} where $\rho_{\min} > 10$.

Additionally to the stability conditions Eqs. (29), (30), and (31) we analyze the surrounding of the zero fixed point ($(\theta_1, \vartheta_1, \vartheta_2) = (0, 0, 0)$) of the system for a given combination of H_{ms}, H_{mt}, H_{ip} on the $(\vartheta_1, \vartheta_2)$ plane, which corresponds to the nullcline of Eq. (25) at $\theta_1 = 0$. For this purpose, we count the

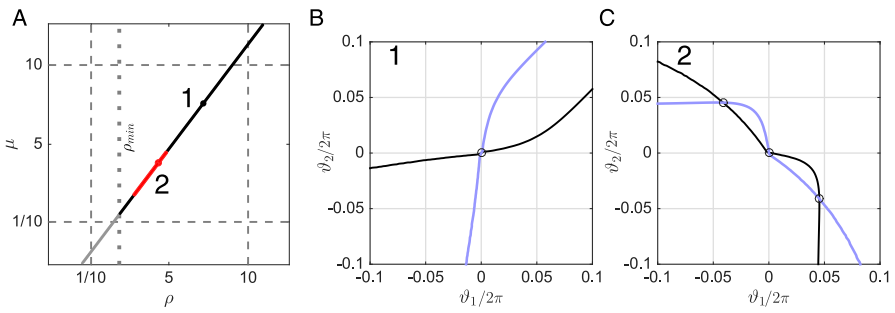

Figure 5: Stability analysis of the solution of the system Eqs. (25),(26), and (27) at the origin $(\vartheta_1, \vartheta_2) = (0, 0)$ and $\theta_1 = 0$. A: The linear relation between the parameters μ and ρ according to Eq. (28). The dashed lines show the borders of physiologically plausible values of the parameters μ and ρ (Eq. (32)), i.e. 1/10 and 10. The vertical dotted line denotes $\rho_{\min}$ (see Eq. (31)). The fixed point at the origin is unstable if $\rho < \rho_{\min}$, shown by the grey line. The black lines are the values of μ and ρ when there is only one stable fixed point at the origin. The red line represents the values of μ and ρ when there are more than one fixed point in the neighborhood of the origin. B and C: An example of the nullclines of Eqs. (26) and (27) for $\theta_1 = 0$ when there is only one and three stable fixed points in the neighborhood of the origin, respectively. The panels B and C correspond to the cases with the parameter values denoted by the points 1 and 2 in the panel A.

number of fixed points in the vicinity of the origin on $(\vartheta_1, \vartheta_2)$ as shown in Fig. 5B and C. We assume that the in-phase solution observed in the experiments is possible if there is only one stable fixed point in the vicinity of the origin, as shown in Fig. 5B. In contrast, if there are several fixed points, as shown in Fig. 5C, a small perturbation of the system could shift the system away from the origin, and thus the stable solution at the origin $(\theta_1, \vartheta_1, \vartheta_2) = (0, 0, 0)$ does not appear in the experiments as the maximum of the distribution of the phase differences.

It needs to be pointed out here that the analyzed system Eqs. (25),(26), and (27) is three dimensional. However, since Eq. (25) does not depend on ϑ_1 and ϑ_2 its nullclines are parallel $(\vartheta_1, \vartheta_2)$ planes. Moreover, given that the contralateral coupling in the mesothoracic ganglion induces in-phase activity, there is only one nullcline of Eq. (25) in the vicinity of the origin, i.e. the nullcline $\theta_1 = 0$. Therefore, we perform the analysis of the three dimensional system on the plane $(\vartheta_1, \vartheta_2)$ for $\theta_1 = 0$.

We count the number of the fixed points – the crossings of the nullclines of Eqs. (26) and (27) for $\theta_1 = 0$ – within the range $-0.1 < \vartheta_1/(2\pi) < 0.1$ and $-0.1 < \vartheta_2/(2\pi) < 0.1$ for all equidistant points along the line Eq. (28) with the step 0.1. If there is only one fixed point at the origin, as shown in Fig. 5B, we draw this part of the $\mu(\rho)$ line with black color, as shown in Fig. 5A, the point 1. On contrary, if there is another pair of fixed points in the vicinity of the origin, as shown in Fig. 5C, then the part of the $\mu(\rho)$ line is plotted with red color, as shown in Fig. 5A, the point 2.

Since the number of the possible coupling combinations is *a priory* large (512), using the results obtained in every step of the analysis we gradually reduce the number of combinations. This is described in the next section.

3 Results

In this section, we present the results obtained by applying the methods discussed in the previous section to the escape type CPGs. First, we study the properties of the coupling function for different coupling types. Next, we define which of these coupling types can be used to describe the intra- and intersegmental couplings. Afterwards, using these results, we analyze the stability of the solutions for the different possible coupling combinations. Finally, we generalize the results by approximating the coupling functions calculated for the escape type CPGs, and establish for an arbitrary type of CPG the coupling properties needed to maintain the results observed in the experiments.

3.1 Coupling functions between escape type CPGs

We calculated the coupling functions H for the different coupling types presented in Fig. 4 using Eq. (8) (or Eq. (9)) for an escape type CPG. The values of the iPRC Z and the membrane potential V where taken from the results of our previous study [22]. The results are shown in Fig. 6A, where every coupling function corresponds to only one synaptic coupling. Please note that the coupling functions of the different coupling types presented in Fig. 6A have various magnitude.

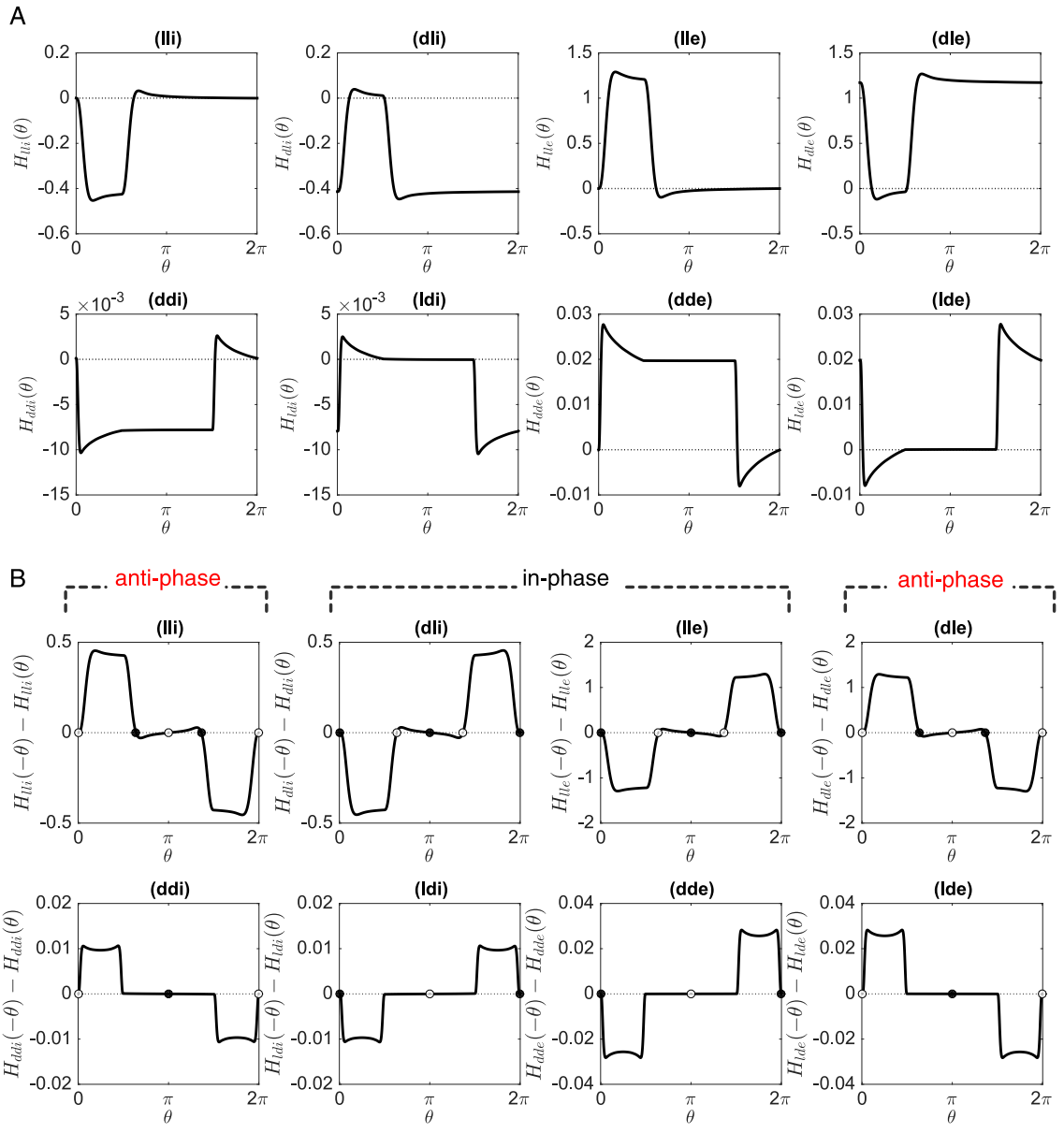

Figure 6: The coupling functions between escape type CPGs for different coupling types. A: The coupling functions H for the different coupling types. The panels are arranged as in Fig. 4A. B: The fixed points and their stability for Eqs. (20) and (21). The filled black and unfilled white circles denote the stable and unstable fixed points, respectively. In all panels the horizontal dotted line denotes zero.

Further, we found the fixed points of the system Eqs. (20) and (21), i.e. for the two symmetric synaptic couplings within a segment, as shown in Fig. 6B. This analysis defines the intrasegmental properties of the coupling types. The cases (dli), (lle), (ldi), (dde) have stable fixed points at $\theta = 0$. The coupling

types (ldi) and (dde) correspond to the case depicted in Fig. 3A. The coupling types (dli) and (lle) have also a stable fixed point at $\theta = \pi$. However, they are surrounded by unstable fixed points at $\theta \approx \varphi_0$ and $\theta \approx 2\pi - \varphi_0$, where φ_0 is the phase of the CPG when the switching between the activities of the depressor and the levator CPG interneurons takes place. These cases correspond to the one presented in Fig. 3C. Furthermore, the derivative of the right hand side of Eqs. (20) and (21) at $\theta = \pi$ is smaller than at $\theta = 0$. As we discussed previously in Sections 2.2.1 and 2.2.3, the chemically activated CPGs have stochastic dynamics, and therefore perturbations always shift the solution of the system Eqs. (20) and (21) from weaker stable fixed points to stronger ones. Thus, we conclude here that for the coupling types (dli) and (lle) the activity of the depressor MNs will appear on average in-phase, namely, at $\theta = 0$.

The cases (lli), (dle), (ddi), (lde) have unstable fixed points at $\theta = 0$. At $\theta = \pi$ the coupling types (ddi) and (lde) have stable fixed points, whereas (lli) and (dle) have unstable ones. Therefore the cases (ddi) and (lde) correspond to the coupling type shown in Fig. 3B. However, in the cases (lli) and (dle) the fixed points at $\theta = \pi$ are surrounded by two symmetric stable fixed points at about $\theta \approx \varphi_0$ and $\theta \approx 2\pi - \varphi_0$. The stable solutions $\theta = \varphi_0$ and $\theta = 2\pi - \varphi_0$ correspond to the cases with zero latency between the activities of the contralateral depressor MNs, i.e. the bursting activity of one depressor MN starts directly after the bursting activity of another (contralateral) depressor MN has ended. Note, that we can distinguish these solutions, because the duration of the depressor and the levator interneurons in the CPG of the stick insect have different durations, namely, $\varphi_0 \neq 0.5$. With respect to our arguments raised in Section 2.2.3 for the coupling types (lli) and (dle) we conclude that the system will symmetrically appear in both states $\theta = \varphi_0$ and $\theta = 2\pi - \varphi_0$, which on average gives a distribution with the maximum at $\bar{\theta} = \pi$, as shown in Fig. 3D. Hence, the coupling types (lli) and (dle), as (ddi) and (lde) on average demonstrate anti-phase solutions.

According to these conclusions the cases (dli), (lle), (ldi), (dde) which have in-phase solutions (Fig. 6B) are the coupling types of the intrasegmental contralateral connections within the mesothoracic ganglion, and the cases (lli), (dle), (ddi), (lde) that demonstrate anti-phase solutions (Fig. 6B) are the ones within the metathoracic ganglion. Furthermore, according to the condition Eq. (30) the coupling types of the intersegmental ipsilateral connections between meso- and metathoracic ganglia are the in-phase coupling cases (dli), (lle), (ldi), and (dde).

3.2 Possible coupling topologies

The results of the previous section help to reduce the number of the possible coupling combinations of the coupling topologies. Thereby, since in each case we have 4 different possible coupling types for the intrasegmental meso- and metathoracic ganglia, and for the intersegmental couplings, in total the number of the possible coupling combinations reduces from 512 to $4 \times 4 \times 4 = 64$. However, we can reduce it even further if we take into account the fact that the coupling functions of the different coupling types significantly differ by magnitude.

In Fig. 7A the magnitude of all coupling types and the relation between them are shown as a table, where the coupling types are sorted by their magnitude. The magnitudes of the coupling types were measured as the maximal variation of the corresponding H functions plotted in Fig. 6A. We consider coupling combinations, where the magnitudes of the couplings differ by more than 15 times, as not physiologically plausible. In other words, the coupling types in the meso- and metathoracic ganglia could be either of the same magnitude or of the one defining the relation between the magnitudes of coupling types shown in Fig. 7A in the right column.

Another restriction to the possible coupling combinations originates from the experimental results [56, 47, 48], which demonstrated that ipsilateral connections are stronger than the contralateral ones. Therefore, we consider only coupling combinations, where the ipsilateral coupling is stronger or equal to the contralateral ones in a ganglion.

Taking this restriction into account all remaining possible combinations are presented in Fig. 7B as a graph. The coupling types are sorted by their magnitudes as in the table of Fig. 7A, and the columns, denoted as meso, meta, and ipsi, correspond to the intrasegmental and intersegmental couplings. The arrows represent possible coupling combinations for given coupling types. Considering ipsilateral couplings to be stronger than contralateral ones in the Fig. 7B only arrows of the same color can be combined: black arrows with black arrows, and blue ones with blue ones. For example, the coupling combinations (dli)-(lli)-(lle), (dli)-(lli)-(dli), and (lle)-(lli)-(lle) are possible, whereas (dli)-(lli)-(dde) and (lle)-(lli)-(dli) are not. By all considered restrictions, the number of possible coupling combinations

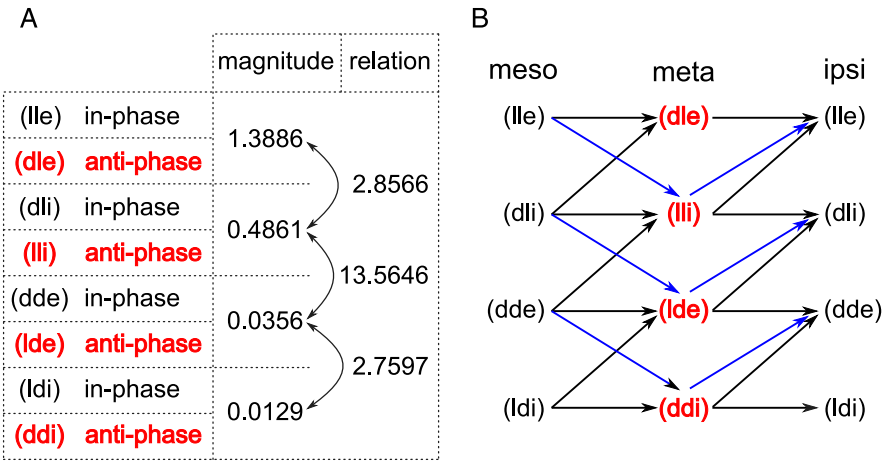

Figure 7: The magnitude of the coupling types and the possible coupling combinations. A: The magnitudes of the coupling types and the relation between them. The magnitudes are defined as the maximal variation of the coupling functions shown in Fig. 6A. B: A graph of the possible coupling combinations. The arrows denote possible coupling types for a given coupling type: only arrows of the same color can be combined (black with black, blue with blue). The labels meso, meta, and ipsi correspond to the intrasegmental contralateral couplings in the meso- and metathoracic ganglia and the intersegmental ipsilateral couplings between ganglia, respectively. The in-phase coupling types are marked with black letters, whereas the anti-phase ones with red letters.

presented in this graph reduces to 15.

3.3 Stability analysis for the complete model

Using the method described in Section 2.3.2 we analyzed the stability of the solution $\theta_1 = 0$ and $\vartheta_1 = \vartheta_2 = 0$ of Eqs. (25), (26) and (27) for the combinations of the coupling functions H_{ms}, H_{mt}, H_{ip} defined by the graph in Fig. 7B. After this analysis only 6 coupling combinations exhibited relevant solutions. They are shown in Fig. 8A. The other coupling combinations had either no solutions, the line $\mu(\rho)$ for these coupling combinations was outside of the considered region, or the line $\mu(\rho)$ was horizontal or vertical (i.e. flat or very steep).

From the analysis of the local stability of the solution $(\theta_1, \vartheta_1, \vartheta_2) = (0, 0, 0)$ (Fig. 8B) one can see that only the three coupling combinations on the left hand side, namely (lle)-(lli)-(lle), (dde)-(lli)-(lle), and (dde)-(ddi)-(dde), have a stable solution for a wide range of the parameter values: there is only one stable solution for $\rho > \rho_{\min}$. By contrast, the three coupling combinations on the right hand side, namely (dli)-(lli)-(dli), (dli)-(lde)-(dli), and (ldi)-(ddi)-(ldi), have some range of the values of μ and ρ, where there is more than one fixed point in the vicinity of the origin (red lines).

According to these results, we conclude that the coupling combinations (lle)-(lli)-(lle), (dde)-(lli)-(lle), (dde)-(ddi)-(dde) are the ones, which could be the underlying neural circuits driving the depressor MN activities seen in the experiments [12] (see Fig. 1). On the other hand, these results are specific to the escape type CPG. Therefore, the local properties of the coupling functions, shown in Fig. 6, determine the appearance of other fixed points around the origin. In the next sections we extend this result to a general approximation of the coupling functions and for arbitrary CPG types.

3.4 Result of the stability analysis for the approximated coupling functions

We approximated the coupling functions shown in Fig. 6 using trigonometric functions by taking into account their form, magnitude and properties around zero, namely the value and the derivative of the coupling functions. Thereby, we set the value of the coupling function at zero equal to zero for the coupling types (lli), (ddi), (lle), (dde); negative for the coupling types (dli) and (ldi), and positive for

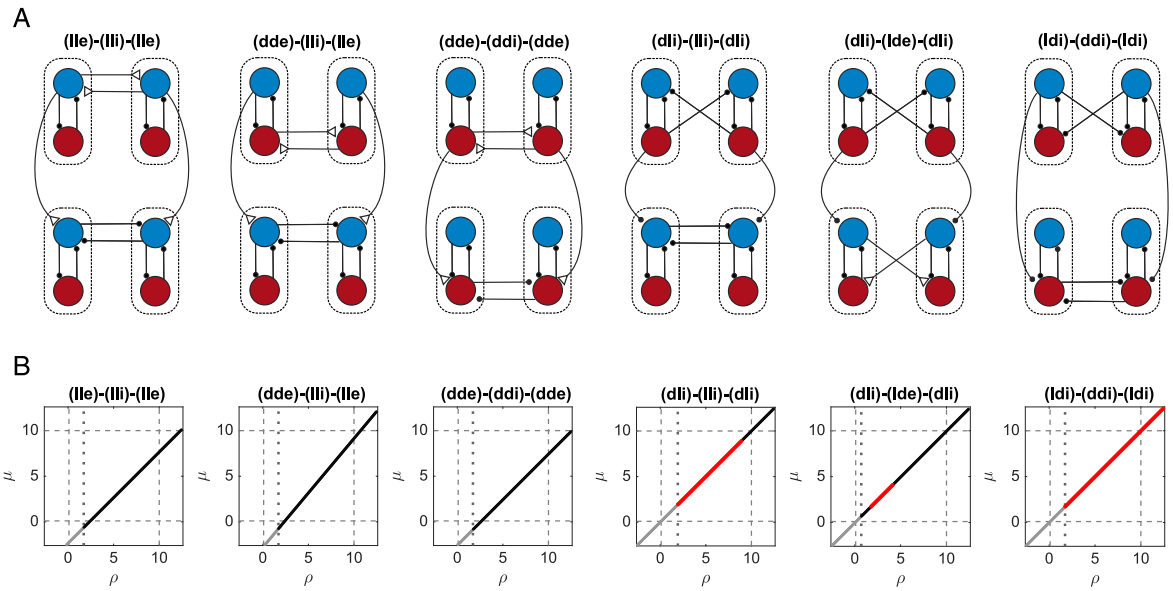

Figure 8: Coupling combinations that have a stable solution $(\theta_1, \vartheta_1, \vartheta_2) = (0, 0, 0)$ for physiologically plausible values of the parameters μ and ρ. A: The scheme of the coupling combinations. B: The linear relation between the parameters μ and ρ, and the stability of the solution $(\theta_1, \vartheta_1, \vartheta_2) = (0, 0, 0)$ for given values of the parameters for the coupling combinations shown in panel A. See Fig. 5 for details.

the coupling types (dle) and (lde). The corresponding formulae are given in C. The results of the approximation are shown in Fig. 9.

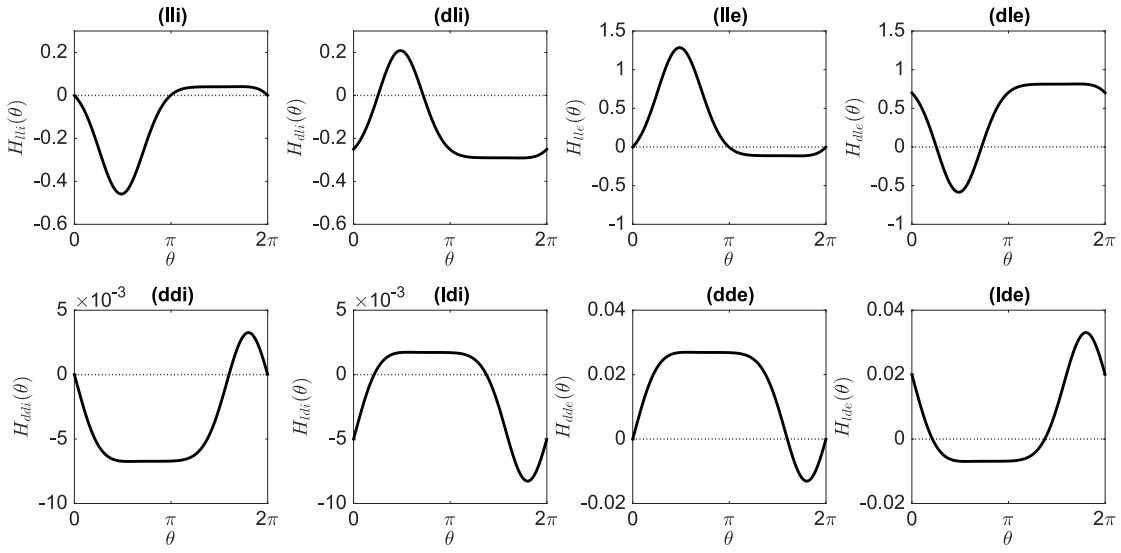

Figure 9: Approximation of the coupling functions shown in Fig. 6. See C for the details of the approximation.

Next, we performed the stability analysis for the approximated coupling functions as discussed in Section 2.3.2 and for the 15 coupling combinations given by the graph in Fig. 7B. The same 6 coupling combinations as in Fig. 8 fulfilled the required conditions. The results of the stability analysis are shown in Fig. 10.

As we expected, due to the approximation and smoothing of the coupling functions the coupling

combinations (dli)-(lli)-(dli), (dli)-(lde)-(dli), and (ldi)-(ddi)-(ldi) have now only one stable solution $(\theta_1, \vartheta_1, \vartheta_2) = (0, 0, 0)$ for the parameter values along the $\mu(\rho)$ line, when $\rho > \rho_{\min}$ (Fig. 10, three panels on the right hand side).

For the coupling combinations (lle)-(lli)-(lle), (dde)-(lli)-(lle), (dde)-(ddi)-(dde) the approximated coupling functions are zero at the origin, which means that the coefficients of the linear equation (28) are zero. Thus, the system Eqs. (25), (26) and (27) has only one stable solution at the origin for any value of μ and $\rho > \rho_{\min}$. These areas appear in the three panels on the left hand side of Fig. 10 as black areas, which are in fact collections of black points. At each point, which represents the parameter values, we found that there is only one intersection of the nullclines of the system Eqs. (25), (26) and (27) at the vicinity of the origin, and that this solution is stable. Similarly, with the parameter values at the grey points in three left panels of Fig. 10, which appear as grey areas, the solution of the system Eqs. (25), (26) and (27) at the origin is unstable.

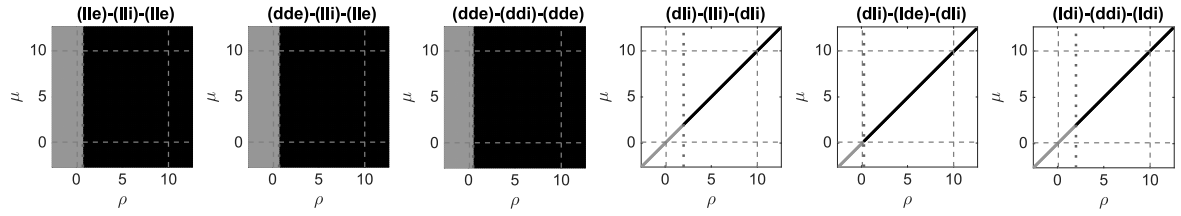

Figure 10: Stability analysis of the coupling combinations with the approximation of the coupling functions shown in Fig. 9. See Fig. 5 for the notation details. The panels have the same order as in Fig. 8B. The black and grey areas on three left panels are in fact collections of black and grey points, which denote stable and unstable fixed points at the origin ($(\theta_1, \vartheta_1, \vartheta_2) = (0, 0, 0)$), respectively. In contrast to the equivalent panels in Fig. 8B, here the $\mu(\rho)$ lines appear as areas, since the coefficients of Eq. (28) are zero and any values of μ and ρ satisfy the linear equation.

3.5 Result of the stability analysis for arbitrary types of CPGs

The theoretical analysis performed in Section 2.2 was derived for any type of synaptic coupling. According to the results of this analysis, the phase relationships between contralateral and ipsilateral depressor MNs observed in the experiments are possible if the contralateral coupling in the mesothoracic ganglion and the ipsilateral intersegmental coupling induce in-phase activity, whereas the contralateral coupling in the metathoracic ganglion induces anti-phase activity. Moreover, the coupling function $H(\theta)$ that corresponds to a specific synaptic coupling must satisfy Eq. (28). This condition only refers to the value of the coupling function at zero ($H(0)$). Therefore, we can restrict our analysis only to these properties of the coupling function and generalize the analysis to any type of synaptic coupling and CPG. These properties of the coupling function can be formatted as a table, shown in Fig. 11A, where the value of the coupling function $H(0)$ can be positive (+), zero (0), or negative (−), and the type of coupling either in-phase (black) or anti-phase (red).

In the previous sections, we analyzed the coupling functions calculated for the case of escape type CPGs. In the table in Fig. 11A the coupling types shown in Fig. 4 are categorized according to the properties of their coupling functions (see Fig. 6). As demonstrated in Fig. 11A, two categories, namely, with $H(0)$ positive and in-phase, and with $H(0)$ negative and anti-phase, which are marked with dashed squares in Fig. 11A, are not to be found in the case of escape type CPGs.

Using this table we can construct a graph, analogous to the one in Fig. 7B, that represents all possible coupling combinations of the intra- and intersegmental couplings. The graph is shown in Fig. 11B. Similar to the graph in Fig. 7B, in Fig. 11B meso and meta denote the intrasegmental contralateral couplings in the meso- and metathoracic ganglia, and ipsi denotes the intersegmental ipsilateral couplings between the segments. The possible coupling combinations that have already been analyzed in the previous chapters are marked with solid arrows; the ones that have not yet been considered with dashed arrows. By constructing the graph we took into account that for meso and ipsi the coupling should induce in-phase activity (black +, 0, − symbols), and for meta anti-phase activity (red +, 0, − symbols).

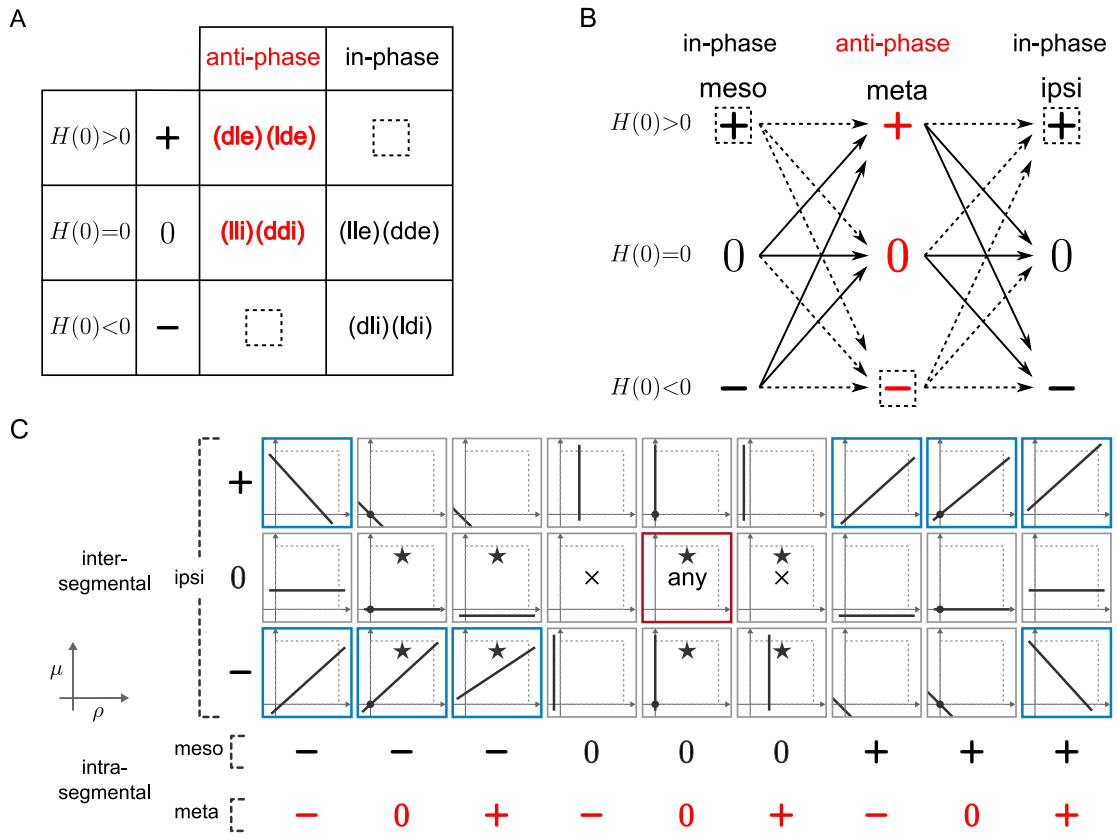

Figure 11: Categorization of the coupling types with respect to the values of the coupling functions and the signs of the derivatives of the coupling functions at zero. A: Tabulated representation of different types of synaptic coupling between CPGs (see Fig. 4) with respect to the properties of their coupling functions calculated for escape type CPGs. The coupling types are categorized according to the results of Section 3.1. The dashed squares mark the cases which have not been observed for the case of escape type CPGs. B: A graph of possible coupling combinations (analogous to the graph in Fig. 7B). The coupling combinations that were considered for the case of escape type CPGs are denoted by solid arrows. The dashed squares and dashed lines mark the coupling types and the coupling combinations not being considered for this case. C: Schematic representation of the linear relation between parameters μ and ρ (Eq. (28)) for all possible coupling combinations derived from the graph in panel B. For every coupling combination the linear relation is presented as thick black line; their crossings with the origin are marked by black circles; the thin dashed grey lines denote the borders of the physiologically plausible values of the parameters μ and ρ; stars (★) denote the cases, which have been considered for the escape type CPGs; no solution cases are marked by crosses (×). Thick blue borders of the small panels mark the coupling combinations that are considered possible, the red border marks the case where any values of μ and ρ are possible, it is also labeled by the word any. Overall, the symbols +, −, and 0 denote the value of the coupling functions being positive, negative, and zero, respectively. The color of the symbols denote the property of the coupling to induce the in-phase (black) and the anti-phase (red) activity.

From Fig. 11B one can see that there are 27 different coupling combinations in total and 8 of them were analyzed for the escape type CPGs. The analysis of the linear relation between the parameters μ and ρ (Eq. (28)) for these 27 coupling combinations is presented in Fig. 11C in schematic form. Every small panel corresponds to one combination from the graph Fig. 11B and shows the linear relation between μ and ρ (Eq. (28)) as in Fig. 5A. The panels are sorted vertically with respect to the values of the intersegmental ipsilateral coupling function (ipsi, $H_{ip}(0)$), and horizontally with respect to the intrasegmental contralateral coupling functions in the meso- and the metathoracic ganglia (meso, $H_{ms}(0)$ and meta, $H_{mt}(0)$). The eight cases, which were considered in the previous sections for the escape type

CPGs, are denoted with stars (★). The symbols +, 0, and −, and their colors have the same meaning as in Fig. 11B.

Similar to the previous analysis, discussed in Section 2.3.2, we consider a coupling combination as being possible, if the line that represents the linear relationship between the parameters μ and ρ, shown as thick black lines in the panels in Fig. 11C, crosses the region of physiologically plausible values of the parameters (thin dashed rectangles defined as $1/10 \leq \mu \leq 10$ and $1/10 \leq \rho \leq 10$). Moreover, as discussed previously in Section 2.3.2 we exclude the cases where the linear relationship is very steep (vertical) or flat (horizontal).

As one can see, in Fig. 11C, there are many coupling combinations that can be excluded. First, we can exclude the flat or steep linear relation between μ and ρ. This takes place if the values of $H_{ip}(0)$ or $H_{ms}(0)$ are very small or if the relation between $H_{ip}(0)$ and $H_{ms}(0)$ is too large. The latter condition is equivalent to the restriction of the relation between the magnitudes of the coupling functions used in Section 3.3 and in Fig. 7. Thus, we exclude all combinations where meso or ipsi are marked with 0 (the special case (0)-(0)-(0) is considered below).

Second, we can exclude the linear relations outside of the dashed rectangles, i.e. the ones that do not have physiologically plausible values of the parameters μ and ρ. To define the conditions when the $\mu(\rho)$ line crosses the region we consider the intersection of the line with the axes:

$$\mu* = \frac{H_{mt}(0)}{H_{ms}(0)}, \text{ when } \rho = 0, \text{ and } \rho* = -\frac{H_{mt}(0)}{H_{ip}(0)}, \text{ when } \mu = 0. \tag{33}$$

Since the relation between the coupling functions is restricted (see Section 3.3 and Fig. 7) the values of $\mu*$ and $\rho*$ are also limited within the given range. Therefore, the $\mu(\rho)$ line crosses the region (I) if $\mu*$ and $\rho*$ have different signs (the three upper right and three lower left blue panels in Fig. 11C) or (II) if $\mu* > 0$ and $\rho* > 0$ (the upper left and the lower right blue panels in Fig. 11C). According to Eq. (33) the case (I) requires $H_{ms}(0)$ and $H_{ip}(0)$ to have the same signs (the line crosses the origin if H_{mt} is zero), whereas the case (II) requires $H_{ms}(0)$ and $H_{mt}(0)$ to have the same signs and $H_{ip}(0)$ a different one.

There is also the special case (0)-(0)-(0) denoted with a red box around the panel and by the word any. In this case the value of the coupling functions $H_{ms}(0)$, $H_{mt}(0)$, and $H_{ip}(0)$ vanishes at zero. Thus, the linear equation (28) has the trivial solution and for any value of the parameters μ and ρ the phase differences are equal to those observed in the experiments. This case was also observed for the escape type CPGs in the previous Section 3.4 (see the three left panels in Fig. 10).

4 Discussion

Chemically activated central pattern generators (CPGs) display stochastic activity. However, as observed in the experiments on depressor MN activity of the stick insect performed by [12] the phase relations of the contralateral depressor MNs arrange around a given value due to the coupling between the CPGs. In this work, we used this adjustment of the phase differences to unravel the type and the properties of the intra- and intersegmental couplings within and between the meso- and metathoracic ganglia of the stick insect. For this purpose, we applied the phase reduction approach to construct a phase-reduced model of the coupled CPGs, and used the results of our previous work [22], where we derived a phase-reduced model for a network of coupled escape type CPGs.

A major advantage of using phase reduction is that it can be applied to any type of oscillatory system. Thereby, in the theoretical part of this work we were able to derive a model in a general form for an arbitrary synaptic coupling and arbitrary type of CPG.

The analysis of the stability of the phase-reduced model Eqs. (16)-(19) revealed that the phase relations observed in the experiments in [12] depend on the relation between the parameters μ and ρ. These parameters describe the relation of the intrasegmental coupling strengths in the metathoracic ganglion and the one in the mesothoracic ganglion and the intersegmental coupling strength between ganglia, respectively.

In [14, 15] the authors found that the intersegmental ipsilateral coupling between all ganglia in locusts maintained a strict in-phase synchronized activity of the depressor MNs. Although, the phase relation between the activities of the intersegmental ipsilateral depressor MN in stick insects was not quantitatively analyzed in [12], the time courses of the electrophysiological measurements presented in their work indicate that the activities also display in-phase synchrony. These results reflect those

revealed by our theoretical analysis, namely that the intersegmental ipsilateral couplings impose in-phase synchrony. Therefore, in the case of interconnected meso- and metathoracic ganglia, the phase relation in the metathoracic ganglion displays in-phase activity only when $\rho > \rho_{\min}$, i.e. the intersegmental coupling imposing in-phase synchrony should overplay the intrasegmental coupling in the metathoracic ganglion, which leads to anti-phase synchrony.

For the interconnected escape type CPG model we found that for some types of synaptic couplings, which demonstrated instability at the origin, a stable fixed point at a value of phase difference of π was observed (the coupling types (ddi) and (lde), see Fig. 6B). However, interestingly, for other connections (the coupling types (lli) and (dle), see Fig. 6B) the solution $\theta = \pi$ was also unstable, but surrounded by two stable solutions, which are located around the phase values where the depressor and the levator CPG interneurons switch their activities, i.e. $\theta = \varphi_0$ and $\theta = 2\pi - \varphi_0$. These solutions correspond to the ones with zero transition latency delay. These results seem to be consistent with other research [57] which also observed a zero transition latency delay in the levator-depressor MN activities in the cockroach. The transition latency was not explicitly analyzed in [12]. However, we concluded in our analysis that the distribution of the phase differences with the maximum at $\theta = \pi$ observed in the experiments in [12] could be the union of two distributions of two stable solutions around the duty factors, namely, $\theta = \varphi_0$ and $\theta = 2\pi - \varphi_0$.

Using the different conditions derived in the theoretical analysis and the restrictions, which arose from physiological plausibility, we could reduce the initial number of 512 possible coupling combinations down to 6 network topologies. Moreover, by approximating the H function of the coupling between the escape type CPGs we could show that the phase relations do not depend on the values of the parameters μ and ρ, if the H functions for all couplings in the network vanish at zero phase difference. Therefore, we hypothesize that the coupling combinations (lle)-(lli)-(lle), (dde)-(lli)-(lle), (dde)-(ddi)-(dde) (Fig. 10) are the network topologies most possibly to be found in insect's neural locomotor circuits composed of escape type CPGs.

On the other hand, the analysis of the model of coupled phase oscillators for an arbitrary type of CPG revealed that other types of coupling topologies, which were not considered in the case of escape type CPGs, could also explain the results of the experiments. Nevertheless, we can conclude that the coupling configuration, with coupling functions $H(0) = 0$ for all inter- and intrasegmental couplings, is the one that does not depend on the variability of the parameters of the system, μ and ρ, i.e. on the relation between the strengths of the couplings and is therefore the most stable one.

The main goal of the current study was to determine the structure of the neural network that drives the levator-depressor MN activities in insect locomotion. We found that the synaptic couplings differ in the different segments (Fig. 8). It is possible, however, that the core structure of the neural circuits in all segments is similar. In particular, the synaptic couplings in one segment could also be present in the other segment, and the phase difference observed in the experiments could be caused by different strengths of the various synaptic couplings in the segment. For example, in the mesothoracic ganglion the synaptic coupling that imposes in-phase synchrony should be stronger than the one that imposes anti-phase synchrony; the opposite should be the case in the metathoracic ganglion. Furthermore, a possible explanation for the absence of a preferred phase difference between rhythmic activities of the contralateral depressor MNs in the prothoracic ganglion, which was also observed in [12], might be an equal strength of the different types of synaptic couplings. The coexistence of two different coupling types and some coupling combinations shown in Fig. 4 do not follow Dale's principle. However, this principle is outdated, as it was shown that neurons can synthesize and release different neurotransmitters. Together with a large variety of postsynaptic receptors in neurons the neurotransmitters determine whether the synapse is excitatory or inhibitory [58].

Despite the fact that the phase relations observed in the experimental work of [12] do not appear in normal walking (fictive locomotion), these phase relations appear to be consistent among animals [57, 14, 15]. Therefore, it is valid to hypothesize that these properties of the fictive locomotion are crucial mechanisms underlying real locomotion. The result of this modeling study can thus be used in future work to investigate the role of these phase relations in the core neural circuit of the motor system in producing normal locomotion in insects. Furthermore, the findings reported in this work can be applied to model other segments, couplings between them and predict different experimental outcomes.

5 Acknowledgements

This work was supported by the DFG Grant DA1953/4-2.

A Infinitesimal phase response curve (iPRC) for the escape type CPG

The iPRC of an oscillating system has the same dimension as the system itself. Every component of the iPRC characterizes the phase response (phase shift) of the system with respect to the input applied to the corresponding component of the system. In Figs. 12A and 12B the iPRC components that correspond to the levator (Z_l) and the depressor (Z_d) interneurons of the CPG are presented. The iPRC of the CPG is calculated as the solution to the corresponding linear adjoint equation subject to the normalization condition (see [22] for details). The same iPRC components enlarged along the y-axis is presented in Figs. 12C and 12D.

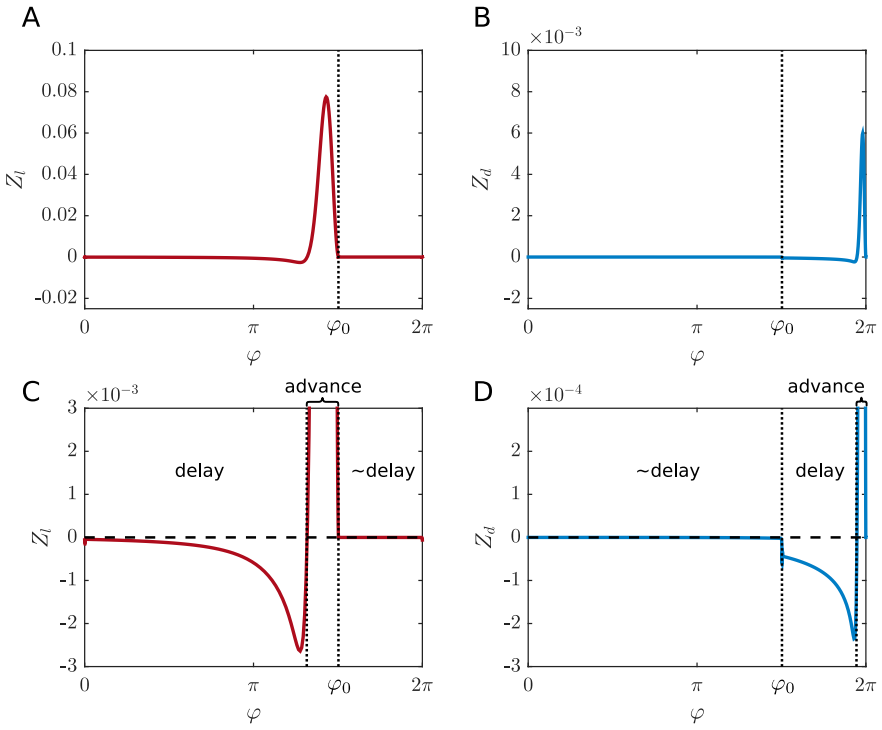

Figure 12: The iPRC of the escape type CPG. A: The iPRC component Z_l that correspond to the levator interneuron of the CPG. B: The iPRC component Z_d that correspond to the depressor interneuron of the CPG. C and D: The same iPRC components as in panels A and B enlarged along the y-axis, with indication of the phase delay and phase advance periods of the iPRC. The text ~delay denotes the period with almost zero (but negative) iPRC, which corresponds to the active state of the interneuron. Vertical dotted lines denote the borders of the phase delay and advance periods. φ_0 is the duty factor of the CPG.

As it was shown by Zhang and Lewis in [33] the iPRC of an escape type CPG is almost zero at the active state of the interneuron of the CPG, and non-zero during the suppressed state, dominated by a large positive peak in the late part of the suppressed state. Since the active interneuron approaches a steady state and remains there until the suppressed interneuron escapes the suppression, any change in the phase of the interneuron in the active state due to perturbation decreases exponentially. This leads to the almost zero (but negative) iPRC in the active state (see [33] for details). By applying different perturbations to an escape type CPG the authors [33] additionally showed that the PRC computed

using this method greatly resembles the iPRC computed using the adjoint method and does not change qualitatively with respect to the strength of the perturbation.

The phase delay and advance periods of the iPRC are shown in Fig. 12C and 12D, the borders between these periods are marked with dotted lines.

B Stability analysis of the system Eqs. (25), (26) and (27)

The Jacobian of the system Eqs. (25), (26) and (27) is

$$J = \begin{pmatrix} \frac{\partial f_0}{\partial \theta_1}, & 0, & 0 \\ \frac{\partial f_1}{\partial \theta_1}, & \frac{\partial f_1}{\partial \vartheta_1}, & \frac{\partial f_1}{\partial \vartheta_2} \\ \frac{\partial f_2}{\partial \theta_1}, & \frac{\partial f_2}{\partial \vartheta_1}, & \frac{\partial f_2}{\partial \vartheta_2} \end{pmatrix}, \tag{34}$$

where

$$\begin{aligned} \frac{\partial f_0}{\partial \theta_1} &= -\mu \frac{\partial H_{ms}}{\partial \theta}(-\theta_1) - \mu \frac{\partial H_{ms}}{\partial \theta}(\theta_1), \\ \frac{\partial f_1}{\partial \vartheta_1} &= -\frac{\partial H_{mt}}{\partial \theta}(-\theta_1 + \vartheta_1 - \vartheta_2) - \rho \frac{\partial H_{ip}}{\partial \theta}(\vartheta_1), \\ \frac{\partial f_1}{\partial \vartheta_2} &= \frac{\partial H_{mt}}{\partial \theta}(-\theta_1 + \vartheta_1 - \vartheta_2), \\ \frac{\partial f_2}{\partial \vartheta_1} &= \frac{\partial H_{mt}}{\partial \theta}(\theta_1 - \vartheta_1 + \vartheta_2), \\ \frac{\partial f_2}{\partial \vartheta_2} &= -\frac{\partial H_{mt}}{\partial \theta}(\theta_1 - \vartheta_1 + \vartheta_2) - \rho \frac{\partial H_{ip}}{\partial \theta}(\vartheta_2). \end{aligned}$$

We find the eigenvalues by setting the determinant of the matrix $(J - \lambda I)$ to zero:

$$\begin{vmatrix} \frac{\partial f_0}{\partial \theta_1} - \lambda, & 0, & 0 \\ \frac{\partial f_1}{\partial \theta_1}, & \frac{\partial f_1}{\partial \vartheta_1} - \lambda, & \frac{\partial f_1}{\partial \vartheta_2} \\ \frac{\partial f_2}{\partial \theta_1}, & \frac{\partial f_2}{\partial \vartheta_1}, & \frac{\partial f_2}{\partial \vartheta_2} - \lambda \end{vmatrix} = \left(\frac{\partial f_0}{\partial \theta_1} - \lambda \right) \begin{vmatrix} \frac{\partial f_1}{\partial \vartheta_1} - \lambda, & \frac{\partial f_1}{\partial \vartheta_2} \\ \frac{\partial f_2}{\partial \vartheta_1}, & \frac{\partial f_2}{\partial \vartheta_2} - \lambda \end{vmatrix} = 0. \tag{35}$$

We now investigate the stability of the solution $\theta_1 = 0$, $\vartheta_1 = \vartheta_2 = 0$. Let us denote

$$A = \frac{\partial H_{mt}}{\partial \theta}(0), B = \frac{\partial H_{ip}}{\partial \theta}(0), C = \frac{\partial H_{ms}}{\partial \theta}(0),$$

then Eq. (35) reads

$$(-2\mu C - \lambda) \begin{vmatrix} -A - \rho B - \lambda, & A \\ A, & -A - \rho B - \lambda \end{vmatrix} = 0.$$

The local eigenvalues are

$$\lambda_1 = -2\mu C, \ \lambda_{2,3} = \frac{1}{2}(\tau \pm \sqrt{\tau^2 - 4\Delta}), \tag{36}$$

where

$$\tau = -2(A + \rho B), \ \Delta = (A + \rho B)^2 - A^2 = 2\rho AB + \rho^2 B^2.$$

Discriminant in Eq. (36) is

$$\tau^2 - 4\Delta = 4(A^2 + 2\rho AB + \rho^2 B^2) - 8\rho AB - 4\rho^2 B^2 = 4A^2,$$

which is always positive. Thus, the system Eqs. (25), (26) and (27) has no imaginary eigenvalues, i.e. has no foci. The local eigenvalues are negative and the zero solution ($\theta_1 = 0$,$\vartheta_1 = \vartheta_2 = 0$) is stable if the following conditions are fulfilled

$$C > 0, \text{ i.e. } \frac{\partial H_{ms}}{\partial \theta}(0) > 0,$$

and

$$\tau \pm \sqrt{\tau^2 - 4\Delta} < 0, \text{ or } \tau \pm \sqrt{4A^2} < 0.$$

For the latter condition, if $A > 0$:

$$-2(A + \rho B) \pm 2A < 0 \rightarrow -A - \rho B \pm A < 0.$$

Therefore, $-\rho B < 0$, or $B > 0$, because $\rho > 0$, and $-2A < \rho B$, thus, $\rho > -2A/B$. For $A < 0$ we have $\tau \mp \sqrt{4A^2} < 0$ which leads to the same conditions:

$$B > 0, \text{ i.e. } \frac{\partial H_{ip}}{\partial \theta}(0) > 0, \text{ and } \rho > -2A/B, \text{ i.e. } \rho > \rho_{\min} = -2\frac{\partial H_{mt}}{\partial \theta}(0)/\frac{\partial H_{ip}}{\partial \theta}(0).$$

C Approximation of the H functions

The H functions for the different coupling types, presented in Fig. 6, were approximated by trigonometric functions that replicate their form and magnitude. The approximation function reads

$$\begin{aligned} \phi(\theta) &= \theta + \sin(\theta - \theta_0) + \sin(\theta_0), \\ \tilde{H}_{jkl}(\theta) &= a + b[\sin(\phi(k\theta + c)) - \sin(\phi(c))], \end{aligned} \tag{37}$$

where $\theta_0 = \pi/4$ and the coefficients k, a, b, c are specific for every coupling type as presented in Table 1. The resulting approximated functions are shown in Fig. 9.

	Coupling types (jkl): (from-to-type)							
Parameters	(lli)	(dli)	(lle)	(dle)	(ddi)	(ldi)	(dde)	(lde)
k	1	1	1	1	-1	-1	-1	-1
a	0	-0.25	0	0.7	0	-0.005	0	0.02
b	-0.25	0.25	0.7	-0.7	0.005	-0.005	-0.02	0.02
c	-0.7	-0.7	-0.7	-0.7	0.2	0.2	0.2	0.2

Table 1: The values of the parameters of the function Eq. (37) for the different coupling types.

References

References

[1] R. M. Alexander, Principles of Animal Locomotion, Princeton University Press, 2003.

[2] G. Wendler, The co-ordination of walking movements in arthropods., Symposium of the Society for Experimental Biology 20 (1965) 229–249.

[3] D. Graham, A behavioural analysis of the temporal organisation of walking movements in the 1st instar and adult stick insect (Carausius morosus), Journal of Comparative Physiology 81 (1) (1972) 23–52. doi:10.1007/BF00693548.

[4] D. Graham, Pattern and Control of Walking in Insects, Advances in Insect Physiology 18 (1985) 31–140. doi:10.1016/S0065-2806(08)60039-9.

[5] P. Holmes, R. J. Full, D. Koditschek, J. Guckenheimer, The dynamics of legged locomotion: models, analyses, and challenges, SIAM Review 48 (2) (2006) 207–304. doi:10.1137/S0036144504445133.

[6] P. S. Katz, Evolution of central pattern generators and rhythmic behaviours., Philosophical transactions of the Royal Society of London. Series B, Biological sciences 371 (1685) (2016) 20150057. doi:10.1098/rstb.2015.0057.

[7] F. Delcomyn, Neural basis of rhythmic behavior in animals., Science 210 (4469) (1980) 492–498. doi:10.1126/science.7423199.

[8] A. Roberts, L. Roberts, B, Neural origins of rhythmic movements, Cambridge University Press, Cambridge, UK, 1983.

[9] D. Wilson, Central nervous control of flight in a locust, Journal Of Experimental Biology 38 (2) (1961) 471–&.

[10] S. Grillner, Control of locomotion in bipeds, tetrapods, and fish, American cancer society, 2011, pp. 1179–1236, first published in print 1981. doi:10.1002/cphy.cp010226.

[11] A. Büschges, J. Schmitz, U. Bässler, Rhythmic patterns in the thoracic nerve cord of the stick insect induced by pilocarpine, The Journal of experimental biology 198 (Pt 2) (1995) 435–56.

[12] C. Mantziaris, T. Bockemühl, P. Holmes, A. Borgmann, S. Daun, A. Büschges, Intra- and intersegmental influences among central pattern generating networks in the walking system of the stick insect, Journal of Neurophysiology 118 (4) (2017) 2296–2310. doi:10.1152/jn.00321.2017.

[13] S. Daun, C. Mantziaris, T. Tóth, A. Büschges, N. Rosjat, Unravelling intra- and intersegmental neuronal connectivity between central pattern generating networks in a multi-legged locomotor system, Plos One 14 (8) (2019) e0220767. doi:10.1371/journal.pone.0220767.

[14] D. Knebel, A. Ayali, H.-J. Pflueger, J. Rillich, Rigidity and flexibility: the central basis of inter-leg coordination in the locust, Front. Neural Circuits 10 (January) (2017) 1–14. doi:10.3389/fncir.2016.00112.

[15] D. Knebel, J. Wörner, J. Rillich, L. Nadler, A. Ayali, E. Couzin-Fuchs, The subesophageal ganglion modulates locust inter-leg sensory-motor interactions via contralateral pathways, Journal of Insect Physiology 107 (January) (2018) 116–124. doi:10.1016/j.jinsphys.2018.03.007.

[16] J. Guckenheimer, P. Holmes, Nonlinear Oscillations, Dynamical Systems, and Bifurcations of Vector Fields, Applied Mathematical Sciences, Springer-Verlag, 1983.

[17] Y. Kuramoto, Chemical Oscillations, Waves, and Turbulence, Vol. 19, Springer Berlin Heidelberg, Berlin, Heidelberg, 1984. doi:10.1007/978-3-642-69689-3.

[18] F. C. Hoppensteadt, E. M. Izhikevich, Weakly connected neural networks, Vol. 126 of Applied Mathematical Sciences, Springer, 1997. doi:10.1007/978-1-4612-1828-9.

[19] J. Proctor, P. Holmes, Reflexes and preflexes: on the role of sensory feedback on rhythmic patterns in insect locomotion, Biological Cybernetics 102 (6) (2010) 513–531. doi:10.1007/s00422-010-0383-9.

[20] J. Proctor, R. P. Kukillaya, P. Holmes, A phase-reduced neuro-mechanical model for insect locomotion: feed-forward stability and proprioceptive feedback., Philosophical transactions. Series A, Mathematical, physical, and engineering sciences 368 (1930) (2010) 5087–5104. doi:10.1098/rsta.2010.0134.

[21] C. Zhang, T. J. Lewis, Robust phase-waves in chains of half-center oscillators, Journal of Mathematical Biology 74 (7) (2017) 1627–1656. doi:10.1007/s00285-016-1066-5.

[22] A. Yeldesbay, T. Tóth, S. Daun, The role of phase shifts of sensory inputs in walking revealed by means of phase reduction, Journal of Computational Neuroscience 44 (3) (2018) 313–339. doi:10.1007/s10827-018-0681-0.

[23] F. K. Skinner, N. Kopell, B. Mulloney, How does the crayfish swimmeret system work? Insights from nearest-neighbor coupled oscillator models, Journal of Computational Neuroscience 4 (2) (1997) 151–160. doi:10.1023/A:1008891328882.

[24] C. Zhang, R. D. Guy, B. Mulloney, Q. Zhang, T. J. Lewis, Neural mechanism of optimal limb coordination in crustacean swimming., Proceedings of the National Academy of Sciences of the United States of America 111 (38) (2014) 13840–5. doi:10.1073/pnas.1323208111.

[25] A. H. Cohen, P. J. Holmes, R. H. Rand, The nature of the coupling between segmental oscillators of the lamprey spinal generator for locomotion: a mathematical model, Journal of Mathematical Biology 13 (3) (1982) 345–369. doi:10.1007/BF00276069.

[26] D. Taylor, P. Holmes, Simple models for excitable and oscillatory neural networks, Journal of Mathematical Biology 37 (5) (1998) 419–446. doi:10.1007/s002850050136.

[27] Z. Aminzare, V. Srivastava, P. Holmes, Gait Transitions in a Phase Oscillator Model of an Insect Central Pattern Generator, SIAM Journal on Applied Dynamical Systems 17 (1) (2018) 626–671. doi:10.1137/17M1125571.

[28] N. Massarelli, G. Clapp, K. Hoffman, T. Kiemel, Entrainment Ranges for Chains of Forced Neural and Phase Oscillators, The Journal of Mathematical Neuroscience 6 (1) (2016) 6. doi:10.1186/s13408-016-0038-9.

[29] E. Couzin-Fuchs, T. Kiemel, O. Gal, A. Ayali, P. Holmes, Intersegmental coupling and recovery from perturbations in freely running cockroaches, Journal of Experimental Biology 218 (2) (2015) 285–297. doi:10.1242/jeb.112805.

[30] S. Daun, J. E. Rubin, I. a. Rybak, Control of oscillation periods and phase durations in half-center central pattern generators: a comparative mechanistic analysis, Journal of Computational Neuroscience 27 (1) (2009) 3–36. doi:10.1007/s10827-008-0124-4.

[31] S. Daun-Gruhn, A mathematical modeling study of inter-segmental coordination during stick insect walking, Journal of Computational Neuroscience 30 (2) (2011) 255–278. doi:10.1007/s10827-010-0254-3.

[32] S. R. Jones, B. Mulloney, T. J. Kaper, N. Kopell, Coordination of cellular pattern-generating circuits that control limb movements: the sources of stable differences in intersegmental phases., The Journal of neuroscience : the official journal of the Society for Neuroscience 23 (8) (2003) 3457–3468. doi:10.1523/JNEUROSCI.23-08-03457.2003.

[33] C. Zhang, T. J. Lewis, Phase response properties of half-center oscillators, Journal of Computational Neuroscience 35 (1) (2013) 55–74. doi:10.1007/s10827-013-0440-1.

[34] S. Daun-Gruhn, T. I. Tóth, An inter-segmental network model and its use in elucidating gait-switches in the stick insect, Journal of Computational Neuroscience 31 (1) (2011) 43–60. doi:10.1007/s10827-010-0300-1.

[35] T. I. Tóth, M. Grabowska, J. Schmidt, A. Büschges, S. Daun-Gruhn, A neuro-mechanical model explaining the physiological role of fast and slow muscle fibres at stop and start of stepping of an insect leg, PLOS ONE 8 (11) (2013) e78246. doi:10.1371/journal.pone.0078246.

[36] T. I. Tóth, J. Schmidt, A. Büschges, S. Daun-Gruhn, A neuro-mechanical model of a single leg joint highlighting the basic physiological role of fast and slow muscle fibres of an insect muscle system, PLOS ONE 8 (11) (2013) e78247. doi:10.1371/journal.pone.0078247.

[37] M. Grabowska, T. I. Tóth, C. Smarandache-Wellmann, S. Daun-Gruhn, A network model comprising 4 segmental, interconnected ganglia, and its application to simulate multi-legged locomotion in crustaceans, Journal of Computational Neuroscience 38 (3) (2015) 601–616. doi:10.1007/s10827-015-0559-3.

[38] T. I. Tóth, M. Grabowska, N. Rosjat, K. Hellekes, A. Borgmann, S. Daun-Gruhn, Investigating intersegmental connections between thoracic ganglia in the stick insect by means of experimental and simulated phase response curves, Biological Cybernetics (109) (2015) 349–362. doi:10.1007/s00422-015-0647-5.

[39] T. I. Tóth, S. Daun-Gruhn, A three-leg model producing tetrapod and tripod coordination patterns of ipsilateral legs in the stick insect, Journal of Neurophysiology 115 (2) (2016) 887–906. doi:10.1152/jn.00693.2015.

[40] T. I. Tóth, E. Berg, S. Daun, Modeling search movements of an insect's front leg, Physiological Reports 5 (22) (2017) 1–17. doi:10.14814/phy2.13489.

[41] T. I. Tóth, S. Daun, Effects of functional decoupling of a leg in a model of stick insect walking incorporating three ipsilateral legs, Physiological Reports 5 (4) (2017) 1–19. doi:10.14814/phy2.13154.

[42] T. I. Tóth, S. Daun, A kinematic model of stick insect walking, Physiological Reports 7 (8) (2019) e14080. doi:10.14814/phy2.14080.

[43] D. Somers, N. Kopell, Rapid synchronization through fast threshold modulation, Biological Cybernetics 68 (5) (1993) 393–407. doi:10.1007/BF00198772.

[44] D. Somers, N. Kopell, Waves and synchrony in networks of oscillators of relaxation and non-relaxation type, Physica D: Nonlinear Phenomena 89 (1-2) (1995) 169–183. doi:10.1016/0167-2789(95)00198-0.

[45] E. M. Izhikevich, Phase Equations for Relaxation Oscillators, SIAM Journal on Applied Mathematics 60 (5) (2000) 1789–1804. doi:10.1137/S0036139999351001.

[46] E. M. Izhikevich, Dynamical Systems in Neuroscience: The Geometry of Excitability and Bursting, no. 1, The MIT Press, 2007.

[47] A. Borgmann, H. Scharstein, A. Büschges, Intersegmental coordination: influence of a single walking leg on the neighboring segments in the stick insect walking system., Journal of Neurophysiology 98 (3) (2007) 1685–1696. doi:10.1152/jn.00291.2007.

[48] A. Borgmann, S. L. Hooper, A. Büschges, Sensory feedback induced by front-leg stepping entrains the activity of central pattern generators in caudal segments of the stick insect walking system., The Journal of Neuroscience 29 (9) (2009) 2972–2983. doi:10.1523/JNEUROSCI.3155-08.2009.

[49] J. Schmitz, A. Büschges, F. Delcomyn, An improved electrode design for en passant recording from small nerves, Comparative Biochemistry and Physiology – Part A: Physiology 91 (4) (1988) 769–772. doi:10.1016/0300-9629(88)90963-2.

[50] U. Bässler, U. Wegner, Motor Output of the Denervated Thoracic Ventral Nerve Cord in the Stick Insect Carausius Morosus, J Exp Biol 105 (1) (1983) 127–145.

[51] J. Goldammer, A. Büschges, J. Schmidt, Motoneurons, DUM cells, and sensory neurons in an insect thoracic ganglion: a tracing study in the stick insect carausius morosus, Journal of Comparative Neurology 520 (2) (2012) 230–257. doi:10.1002/cne.22676.

[52] G. Laurent, M. Burrows, Distribution of intersegmental inputs to nonspiking local interneurons and motor neurons in the locust, The Journal of Neuroscience 9 (9) (1989) 3019–3029. doi:10.1523/JNEUROSCI.09-09-03019.1989.

[53] G. Laurent, M. Burrows, Intersegmental interneurons can control the gain of reflexes in adjacent segments of the locust by their action on nonspiking local interneurons, The Journal of Neuroscience 9 (9) (1989) 3030–3039. doi:10.1523/JNEUROSCI.09-09-03030.1989.

[54] T. Kiemel, A. H. Cohen, Estimation of coupling strength in regenerated lamprey spinal cords based on a stochastic phase model, Journal of Computational Neuroscience 5 (3) (1998) 267–284. doi:10.1023/A:1008835011799.

[55] T. Kiemel, K. M. Gormley, L. Guan, T. L. Williams, A. H. Cohen, Estimating the strength and direction of functional coupling in the lamprey spinal cord, Journal of Computational Neuroscience 15 (2) (2003) 233–245. doi:10.1023/A:1025868910179.

[56] B. C. Ludwar, Modulation of Membrane Potential in Mesothoracic Moto- and Interneurons During Stick Insect Front-Leg Walking, Journal of Neurophysiology 94 (4) (2005) 2772–2784. doi:10.1152/jn.00493.2005.

[57] I. David, P. J. Holmes, A. Ayali, Endogenous rhythm and pattern-generating circuit interactions in cockroach motor centres, Biol. Opt. 5 (9) (2016), 1229-1240, doi:10.1242/bio.018705.

[58] G. Burnstock, Cotransmission, in: Reference Module in Biomedical Sciences, Elsevier, 2014, pp. 5–19. doi:10.1016/B978-0-12-801238-3.04564-5.